Hypersonic nozzle for laser-spectroscopy studies at 17 K characterized by resonance-ionization-spectroscopy-based flow mapping

Ferrer, R.; Verlinde, M.; Verstraelen, E.; Claessens, A.; Huyse, M.; Kraemer, S.; Kudryavtsev, Yu.; Romans, J.; Van den Bergh, P.; Kalikmanov, V.I.

DOI
10.1103/PhysRevResearch.3.043041

Publication date
2021

Document Version
Final published version

Published in
Physical Review Research

Hypersonic nozzle for laser-spectroscopy studies at 17 K characterized by resonance-ionization-spectroscopy-based flow mapping

R. Ferrer,* M. Verlinde, E. Verstraelen, A. Claessens, M. Huyse, S. Kraemer, Yu. Kudryavtsev, J. Romans, P. Van den Bergh, P. Van Duppen, and A. Zadvornaya
KU Leuven, Instituut voor Kern- en Stralingsfysica, Celestijnenlaan 200D, B-3001 Leuven, Belgium

O. Chazot and G. Grossir
Aeronautics & Aerospace Dept., von Karman Institute, Chaussée de Waterloo, 72 1640 Rhode-St-Genèse, Belgium

V. I. Kalikmanov
Department of Engineering Fluid Mechanics, University of Twente, Drienerlolaan 5, 7522 NB Enschede, The Netherlands; Department of Geosciences, Delft University of Technology, Stevinweg 1, 2628 CN Delft, The Netherlands and Twister Supersonic Gas Solutions, Einsteinlaan 20, 2289 CC, Rijswijk, The Netherlands

M. Nabuurs and D. Reynaerts
KU Leuven, Department of Mechanical Engineering, Celestijnenlaan 200F, B-3001 Leuven, Member of Flanders Make, Belgium

(Received 20 April 2021; revised 6 May 2021; accepted 10 September 2021; published 15 October 2021)

The in-gas-jet laser spectroscopy method relies on the production of uniform and low-temperature gas jets to fully resolve the atomic hyperfine structure and efficiently determine fundamental nuclear properties of short-lived isotopes from, e.g., the hardly accessible actinide and transactinide elements. In this article we present the studies devoted to designing, producing, and characterizing the flow properties of a convergent-divergent (de Laval) hypersonic nozzle with a superior performance for laser spectroscopy applications. A novel flow mapping technique, based on resonance ionization spectroscopy (RIS), has been employed to characterize the local flow properties of an argon gas jet formed by this nozzle, revealing a 61.5-mm long, highly collimated atomic jet at a uniform low temperature of 16.6(5) K [Mach 8.11(12)] that will enable laser spectroscopy experiments on heavy-exotic nuclei with an unprecedented spectral resolution and a high efficiency. These results have been compared with those obtained by planar laser induced fluorescence spectroscopy (PLIFS) studies and show a good agreement between the two techniques and a significant improvement in efficiency of the RIS mapping method with respect to PLIFS. The data are compared to state-of-the-art fluid-dynamics calculations that were carried out to obtain the nozzle contour and simulate its performance, as well as to explain the observation of a possible onset of argon nucleation.

DOI: 10.1103/PhysRevResearch.3.043041

I. INTRODUCTION

In-gas laser ionization and spectroscopy (IGLIS) is the technique of choice—either in the in-gas-cell laser spectroscopy [1,2] or the detected resonance ionization spectroscopy (RADRIS) [3,4] methods—to study atomic (chemical) properties as well as nuclear ground- and isomeric-state properties of heavy exotic nuclei. An example can be found in the actinide elements, with atomic number ranging from $Z = 89$–103, which are produced in heavy-ion induced fusion-evaporation reactions at accelerator facilities and thermalized in a high-pressure buffer gas cell. Information on atomic levels and ionization potentials or nuclear electromagnetic moments, spins, and charge radii of the isotopes in the actinide region are of particular interest. On the one hand, relativistic effects start here to notably influence the electronic structure of the atom [5], and on the other, a detailed knowledge of their underlying nuclear structure can be used to test and refine nuclear-model predictions of the exact location of the next proton or neutron shell closures that has been associated with long-lived super-heavy nuclei [6]. These studies are essential to gain insight in the atomic and nuclear properties governing the super-heavy elements (SHE).

Combining the high ionization efficiency and selectivity of resonance ionization spectroscopy with the high-spectral resolution features of the low-temperature and low-density supersonic gas jet environment, the in-gas-jet spectroscopy method [7] has proven to overcome the intrinsic low-spectral resolution associated with typical broadening mechanisms present in a buffer gas environment at room temperature. Successful reduction of collisional and Doppler broadening effects, make in-gas-jet laser spectroscopy a promising

*Rafael.Ferrer@kuleuven.be

method to study heavy nuclei with an order of magnitude higher precision and without loss in efficiency, in comparison to the conventional IGLIS technique. An example of its applicability on the ^{214,215}Ac isotopes has been reported in Ref. [8]. Current experimental campaigns at the Helmholtzzentrum für Schwerionenforschung (GSI) [9] or future experiments planned at new radioactive ion beam (RIB) facilities such as S3-LEB at SPIRAL2, GANIL (France) [10], will also apply the in-gas-jet spectroscopy method to study the atomic and nuclear structure of actinides.

Ever since the first off-line demonstration [7], the in-gas-jet spectroscopy method has been further characterized and optimized in a dedicated new IGLIS laboratory [11]. Among the different research subjects, such as the development of a Fourier limited pulsed-dye amplifier suited for high-resolution laser spectroscopy experiments [12] or the efficient capture and transport of photo-ions by a radio-frequency quadrupole ion guide system [13], the production of uniform and collimated jets at very low temperatures has been studied. Gas jets with these characteristics are important, firstly to provide the best spectral resolution by reducing the Doppler broadening associated with the jet temperature and divergence, and secondly, to maximize the efficiency by optimally matching the temporal and spatial overlap of the gas jet with the laser beams. First studies in this respect [14] aimed to design a nozzle with a high Mach number $M = 8.5$, limited by the typical pumping capacity of the vacuum systems at RIB facilities. In these investigations, however, we could only produce gas jets of such characteristics by nozzles with a maximum average Mach number $M = 4.7(2)$ mainly due to software and hardware limitations that prevented proper calculations of nozzle contours under a correct treatment of viscous effects.

The design of high-Mach-number nozzles (hypersonic, $M > 5$) is complicated by the increasing influence of viscous effects on the core of the nozzle flow. Boundary layer thicknesses scale with the square of the edge Mach number in the hypersonic regime [15] leading to the development of extremely thick boundary layers along the nozzle walls. In the most extreme cases, this can lead to an entirely viscous flow within the nozzle, preventing the nozzle from reaching the targeted high-Mach number by the nozzle exit. Appropriate viscous corrections are therefore required.

In Ref. [14], we carried out quantitative measurements of the gas jets produced with the various nozzle designs by the planar laser induced fluorescence spectroscopy (PLIFS) method. Spectroscopy of the $^2S_{1/2}$ - $^2P_{1/2}$ transition at 327.49 nm in copper atoms seeded in argon was used to extract local flow properties such as temperature, velocity, and relative density, and deduce the Mach number distribution. The relatively simple hyperfine spectra obtained from atomic spectroscopy, in contrast to molecular spectroscopy, enables the extraction of local flow properties with a high accuracy, as the width of the spectral lines is related to the temperature, the velocity can be measured through the Doppler shift, and the total intensity of the collected light is related to the density. However, PLIFS, like other nonintrusive flow visualization methods currently in use, such as particle image velocimetry (PIV), laser Doppler velocimetry (LDV), or filtered Reyleigh scattering (FRS), to name a few (see [16] and references therein for a detailed overview of flow visualization methods), relies on the detection of fluorescence (or scatter light) that usually results in a poor efficiency of the method and thus, in long measurements times to achieve, for instance, the reported relative accuracy in these measurements of 3×10^{-3} and 7×10^{-2} for the local flow velocities and temperatures, respectively.

In this article, we propose and report an alternative nonintrusive method to characterize local flow properties of supersonic/hypersonic gas jets that is based on resonance ionization spectroscopy (RIS). Unlike other conventional flow visualization methods, the RIS mapping method takes advantage of the ionization of particles seeded in the gas flow to boost its overall efficiency by significantly improving the collection and detection efficiency as compared to light-detection methods. Furthermore, owing to the mass filtering potentiality, it provides isotope-separated samples of seeded atoms that simplify the spectra and enable a more precise analysis of the obtained linewidths to deduce the flow properties. We have used the RIS mapping method to characterize the local flow properties of a newly designed contoured nozzle aiming at Mach 8.5. The new nozzle geometry was determined using the HYPNOZE design code of the von Karman Institute for Fluid Dynamics (VKI), which first led to the definition of an inviscid contour, followed then by a viscous correction to yield the required free-stream flow conditions. This correction to the inviscid contour was inferred from a Navier-Stokes laminar flow solution from which the boundary layer displacement thickness could be evaluated.

An extensive campaign of studies has been carried out to design, manufacture, and characterize the performance of the new hypersonic nozzle. The results extracted by the RIS flow mapping method are compared with those obtained by PLIFS and are found to be in good agreement. The two methods show complementary features that suggest a combination of both, PLIF for relative density profiles and RIS for temperature and velocity measurements, as the most efficient way to characterize the local flow properties of a hypersonic gas jet. Furthermore, the experimental results are found to be in good agreement with computational fluid dynamics (CFD) predictions and reveal a gas jet of high radial and axial homogeneity with an average Mach number of $M = 8.11(12)$ along the first 61.5 mm after the nozzle exit. This translates in an average minimum temperature of the jet core of 16.6(5) K for a stagnation temperature of 380 K. These jet features are ideal for laser spectroscopy experiments of actinide elements produced at RIB facilities as a full spatial and temporal overlap of the gas jet with laser beams will result in optimal ionization efficiency and reduction of the broadening mechanisms affecting the spectral line width. The low cryogenic temperatures, however, might carry a negative side effect for future in-gas-jet laser spectroscopy studies as condensation of argon atoms is shown to decrease the designed Mach number by 25%. A systematic study of the Mach number evolution for different stagnation temperatures T_0 at a stagnation pressure $P_0 = 300$ mbar points to an onset of argon nucleation at $T_0 \approx 380$ K.

The article is organized as follows: In Sec. II we report on the theoretical and numerical calculations performed to obtain the nozzle contour and the technical details related to the nozzle manufacturing. In Sec. III the two experimental methods applied to characterize the flow properties are

presented with particular emphasis on the recently developed RIS mapping method. The results are presented and discussed in Sec. IV, followed by a new set of fluid dynamics calculations, in Sec. V, to describe the experimental observation of the proposed onset of argon nucleation. Finally, a summary and outlook is given in Sec. VI.

II. NOZZLE CONTOUR: STATE-OF-THE-ART CALCULATIONS AND ACCURATE MACHINING

To overcome the computational limitations that prevented us from achieving uniform high Mach number flows in our previous studies [14], we made use this time of theoretical methods and numerical tools employed at the VKI. An adaptation of the HYPNOZE nozzle design code, such as considering argon as carrier gas and applying a viscous correction for laminar boundary layers, was initially carried out to make it suitable to the typical experimental conditions in IGLIS studies.

The design conditions aiming at a Mach 8.5 axisymmetric contoured nozzle were set such that argon, behaving as a perfect gas, was assumed at stagnation conditions (i.e., those in the gas cell) of pressure $P_0 = 300$ mbar and temperature $T_0 = 296$ K at the nozzle inlet. The nozzle walls were kept isothermal at a temperature $T_w = 294$ K in the calculations according to the results obtained in a measurement of the temperature of the nozzle walls during gas expansion. A small PT-100 sensor separated from the inner contour by a layer only 1-mm thick of nozzle material showed a fast decrease of the initial temperature in the first minutes after gas expansion that slowly converged after a few hours with a net temperature decrease of ∼1.5 K, revealing thus that the gas expansion does not significantly change the working temperature of the nozzle. The flow was considered to be laminar and the nozzle throat diameter was set to 1 mm. The latter value is based on the compromised choice between the mass flow rate through the nozzle to provide a fast evacuation of the gas cell and the pumping speed capacity of typical pumping systems at RIB facilities.

A. Determination of the contour

The method of characteristics [17] was used first to design an inviscid contour. This method relies on the definition of a continuous and monotonic Mach number distribution along the nozzle axis ending up with the target free-stream Mach number for the nozzle [18,19]. Following such an approach, an infinite number of inviscid contours can be identified that will all yield, theoretically, the same exit flow conditions (uniform and parallel flow). These can be obtained by selecting different values for the major contour design parameters. Among all theoretical designs available, some offer better performances than others. That is so, because the method of characteristics does not account for possible flow separation, thermal exchange with the nozzle walls, or the thick hypersonic boundary layers, which all contribute to degrading the flow quality at the nozzle exit. The following design parameters were selected based on recommendations from the literature. R indicates how rapidly the nozzle opens near the throat and $R = R_c/r = 6$, where R_c is the throat radius of curvature and $r = 0.5$ mm is the nozzle throat radius, the maximum nozzle opening angle $\omega = 11^\circ$ and the characteristic length $X = 9.126$ mm for the transition segment between the end of the radial flow region and the beginning of the uniform flow region, as defined in Ref. [19]. From these parameters, a unique set of boundary conditions (Mach number and local flow angle) can be determined. The nozzle contour associated to the resulting Mach number distribution was finally determined in a stepwise manner using the methods of characteristics. The resulting inviscid nozzle contour is illustrated in Fig. 1 (dashed line).

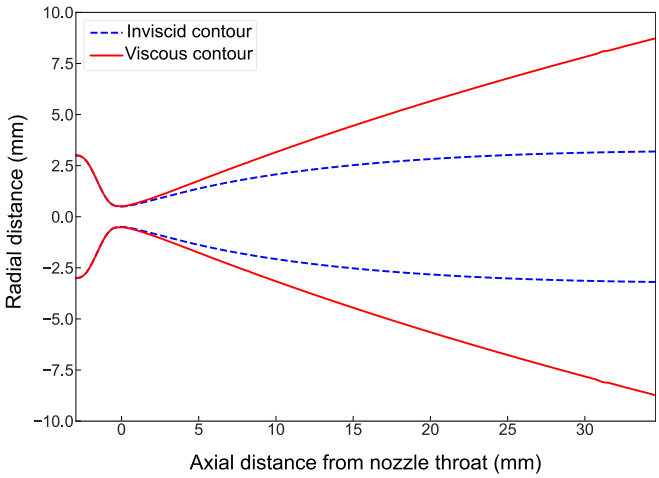

FIG. 1. Inviscid (dashed line) and viscous (solid line) contours for a Mach 8.5 nozzle for a set of design parameters from the literature. The length of the viscous contour is found to maximize the uniform core flow (see text for details).

The viscous correction on the inviscid contour was obtained from numerical flow simulations. First, a numerical solution for a laminar viscous flow was obtained on the inviscid contour. The corresponding boundary layer displacement thickness δ^* was determined everywhere along the contour and added to the inviscid contour in order to obtain an initial viscous contour such that $y_{\text{viscous}}(x) = y_{\text{inviscid}}(x) + \delta^*(x)$, with y and x indicating respectively the vertical and horizontal dimensions from the nozzle throat (cf. Fig. 1).

A second numerical solution was obtained using now the modified contour. The boundary layer displacement thickness δ^* was again determined everywhere along the contour and added to the original inviscid contour. The procedure was repeated iteratively until convergence. The resulting viscous contour is illustrated in Fig. 1 (solid line). For the present set of stagnation conditions and the present geometry, the boundary layer displacement thickness can be described by a function composed of an exponential growth close to the throat followed by a linear one further downstream.

In view of these results, we can at this point draw an important conclusion. The use of low stagnation pressures ($P_0 = 300$ mbar) leads to very low Reynolds numbers Re during the following nozzle expansion. In these conditions, very thick boundary layers develop along the nozzle walls and lead to a viscous contour significantly different from the inviscid one, and also relatively unusual for a contoured nozzle. This effect might explain why only nozzles with a low Mach

number (M $<$ 5) and somewhat uniform and collimated flows could be obtained in our former studies, in which no viscous correction was applied. The viscous effects also contribute to enlarge slightly the throat diameter of the nozzle and the nozzle opening angle, which are found to be $d = 1.029$ mm and $\omega = 16.6^{\circ}$.

The length of the viscous contour can be shortened slightly in order to maximize the dimensions of the uniform core flow. This optimization stems from the fact that from a given location the growth rate of the boundary layer is more rapid than the growth rate of the contour [20]. For the present nozzle, the contour was limited to an axial distance $x = 34.58$ mm as shown in Fig. 1. The use of a longer nozzle would only reduce the size of the inviscid core flow.

It is important to note that the present viscous correction was derived for a specific set of initial conditions. Nozzle operation with significantly different stagnation conditions or with a different gas such as helium, might be associated with dissimilar viscous effects with possible consequences on the nozzle flow uniformity. For such cases, a new set of CFD calculations would be required to check the expected nozzle performance.

B. Flow simulations

The compressible perfect gas Navier-Stokes equations were solved to the second order for a laminar flow expanding within the obtained viscous contour by CFD calculations. The numerical results for the nozzle flow were first compared to the theoretical results issuing from the method of characteristics. The presence of extremely thick boundary layers was clearly noticeable. In spite of these significant viscous effects, the inviscid region remained in good agreement with the ideal inviscid flow solution. A satisfactory agreement between the theory and the CFD results is observed for the pressure, the temperature, the flow velocity, and the local Mach number within the nozzle. Additional numerical simulations were performed with the inclusion of a simplified test chamber, modeling the IGLIS gas cell chamber, following the nozzle. A low background pressure P_{bg} in the test chamber led to an underexpanded flow configuration ($P_e > P_{bg}$, with P_e the pressure at the nozzle exit) and large Mach numbers along the nozzle axis. Ultimately, shock waves were also present along the nozzle axis. For larger values of P_{bg}, an overexpanded flow configuration ($P_e < P_{bg}$) was observed with shock waves located very close to the nozzle exit. A careful adjustment of P_{bg} generates a rather uniform hypersonic flow in the test chamber, indicating that a satisfactory performance of the nozzle requires a precise tuning of P_{bg}.

The uniformity of the jet in the test chamber for the flow density and the Mach number distributions is illustrated in Fig. 2 for the specific case in which $P_{bg} = 0.13$ mbar. The flow uniformity for this background pressure is excellent in the region immediately downstream of the jet (34.5 mm $< x <$ 60 mm, x being the axial distance from the nozzle throat) with an average Mach number $M = 8.4$ and with axial variations smaller than 3.4% for the density and than 1.2% for the Mach number. Weak shock waves are present in the flow further downstream that contribute to decrease the flow uniformity in these regions, resulting in an average Mach number $M = 8.2$ (for 34.5 mm $< x <$ 185 mm).

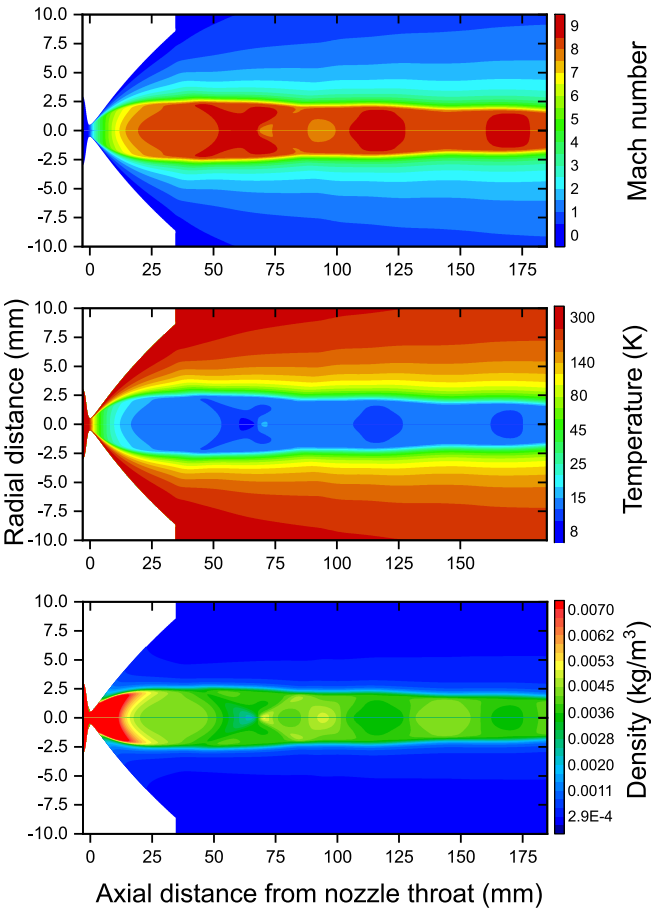

FIG. 2. 2D maps providing detailed flow conditions for the density (bottom), temperature (middle), and Mach number (top) for stagnation conditions $P_0 = 300$ mbar and $T_0 = 294$ K in the gas cell and $P_{bg} = 0.13$ mbar in the test chamber.

C. Manufacturing

The calculated contour was machined with a high accuracy and excellent surface finish to rule out any observed deviations of the simulated flow properties due to mechanical imperfections. A precision turning machine with custom-made turning tools, as described in Ref. [14], was used to manufacture a number of nozzles. This time we chose brass as the nozzle material for its easy-to-machine properties and a nondestructive replica molding technology for monitoring the surface topography [21]. Unlike in our previous studies, in which we had to cut in half the nozzles to measure the surface roughness of the contours, with the molding technique [22] we could make replications of the nozzle inner surface that were subsequently analyzed with a Sensofar 3D microscope. The nozzle geometrical accuracy was measured with a Werth VideoCheck HA coordinate measuring machine. The fabrication process followed an iterative procedure until the desired tolerances were reached. That is, the contour was repeatedly machined and subsequently measured on the Werth coordinate machine until the contour deviations were acceptable. In total five

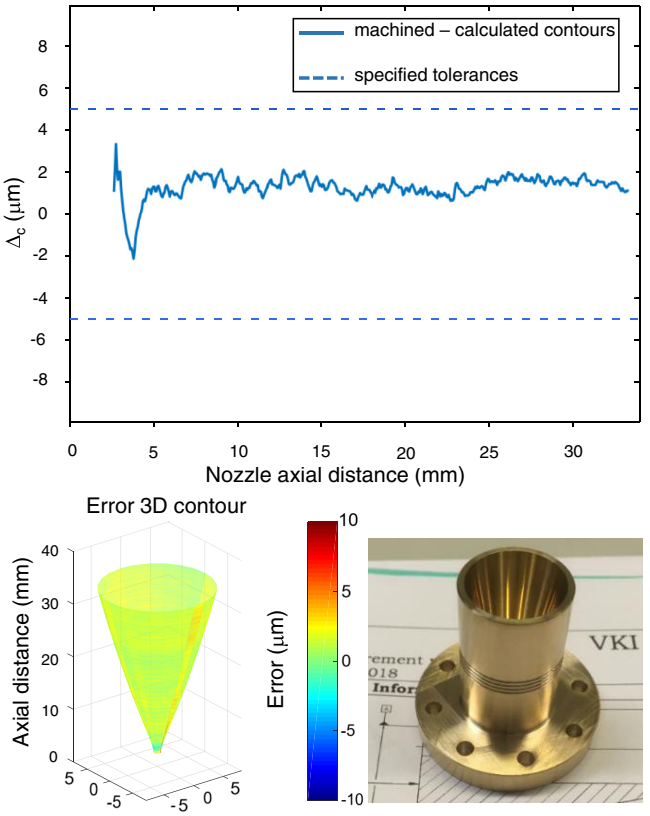

FIG. 3. (Top panel) Deviation between the machined and the calculated nozzle contours Δ_c. The dashed lines indicate the specified upper limit precision. (Bottom panel) 3D visualization of the machined contour error shown above and a picture of the manufactured nozzle in brass.

nozzles were manufactured in this way, of which only two were machined within the aimed specifications of $\Delta_c = \pm 5\ \mu$m for the contour accuracy, i.e., for the maximal allowed difference between the manufactured and the calculated nozzle contours, and $R_a \leqslant 0.1\ \mu$m for the surface roughness. Figure 3 illustrates the deviation in the contour of one of such manufactured nozzles with respect to that calculated. This nozzle was used in all the characterization studies presented in this article. The surface roughness close to the throat, in the middle and at the exit of the nozzle was measured to be R_a =100, 100, and 80 nm, respectively, and the throat diameter was found to be 1.0275(10) mm.

III. EXPERIMENTAL METHODS

We performed an extensive series of measurements to characterize the flow properties of the gas jets produced by the hypersonic nozzle. First, the PLIF method was applied to record density profiles and obtain the matched flow conditions for the nozzle, which enabled the best pressure conditions to form a collimated, uniform jet. This information was then used to perform RIS studies and extract detailed information of its local flow properties, such as the velocity and temperature, which could finally be utilized to map the evolution of the Mach number along the hypersonic jet. The PLIFS method was finally applied and the results used as benchmark to test the validity of the new RIS mapping method.

PLIF(S) was performed as in previous measurements [14] and for that reason we will not go here into details about the experimental setup and the data collection. On the contrary, the RIS mapping method has been applied for the first time to obtain the aforementioned flow properties and its main characteristics will be outlined in the following.

A. The RIS mapping method

A drawback of the PLIFS method is the long measurement times needed to extract local flow properties with high accuracy. This is caused mainly by the low sensitivity and overall efficiency of the method that also makes it difficult to realize the measurements under constant experimental conditions. To overcome these limitations, a new RIS mapping method was implemented and applied at the IGLIS laboratory to characterize the performance of de Laval nozzles. A schematic overview of the experimental setup can be found in Fig. 4. In this method, as in PLIFS, copper atoms are produced by resistive heating of a thin filament (F1 or F2) in the gas cell filled with argon at a typical stagnation pressure of $P_0 = 300$ mbar. Argon as carrier gas, seeded with copper atoms, is then evacuated through the nozzle under study. This, in turn, produces a hypersonic gas jet when the flow adiabatically expands in the gas cell chamber kept at a lower background pressure P_{bg}. By adjusting P_{bg} to match the pressure of the gas jet at the nozzle exit P_e, i.e., $P_e/P_{bg} = 1$, a well-collimated jet is formed whose properties remain stable over a distance many times larger than its diameter.

Two laser beams are allowed to intersect the jet in different geometries to stepwise excite and ionize at 10 kHz pulse repetition rate the seeding atoms in the argon outflow. The first laser (Λ_1) excites the atoms from the ground state to an excited state at 30535.23 cm^{-1} (see ionization scheme in Fig. 5). This corresponds to a laser radiation obtained after second harmonic generation (SHG) at a vacuum wavelength $\lambda_1 = 327.4905$ nm that can be produced in two different ways depending on the application. If we want to study the relative density in the jet, a Nd:YAG-pumped dye laser ($\Delta_\nu =$ 3.4 GHz), referred to as broadband Laser 1, Λ_1^{BB}, is utilized at an average power of 300 mW. If, on the other hand, the velocity or temperature of the jet is to be measured, we make use of a laser with a narrower bandwidth ($\Delta_\nu \sim 100$ MHz), which is obtained by the amplification of a single-mode diode laser in a pulsed dye amplifier (PDA). The PDA was typically pumped by the Nd:YAG laser also pumping Λ_1^{BB} but it can also be pumped by a single-longitudinal-mode Nd:YAG laser to obtain Fourier-limited single-mode laser pulses [12]. We refer to this laser hereafter as narrow-band Laser 1, Λ_1^{NB}. As laser spectroscopy measurements are required to measure local flow properties, the power density of this laser must be kept down to about 0.5 μW/mm^2 to minimize linewidth broadening. This was always controlled by performing reference scans at the start of a measurement run, whereby the onset of power broadening was defined by measuring the total spectral resolution for decreasing laser intensities. The second step laser (Λ_2), also a Nd:YAG pumped dye laser at a vacuum wavelength obtained after SHG $\lambda_2 = 287.98$ nm,

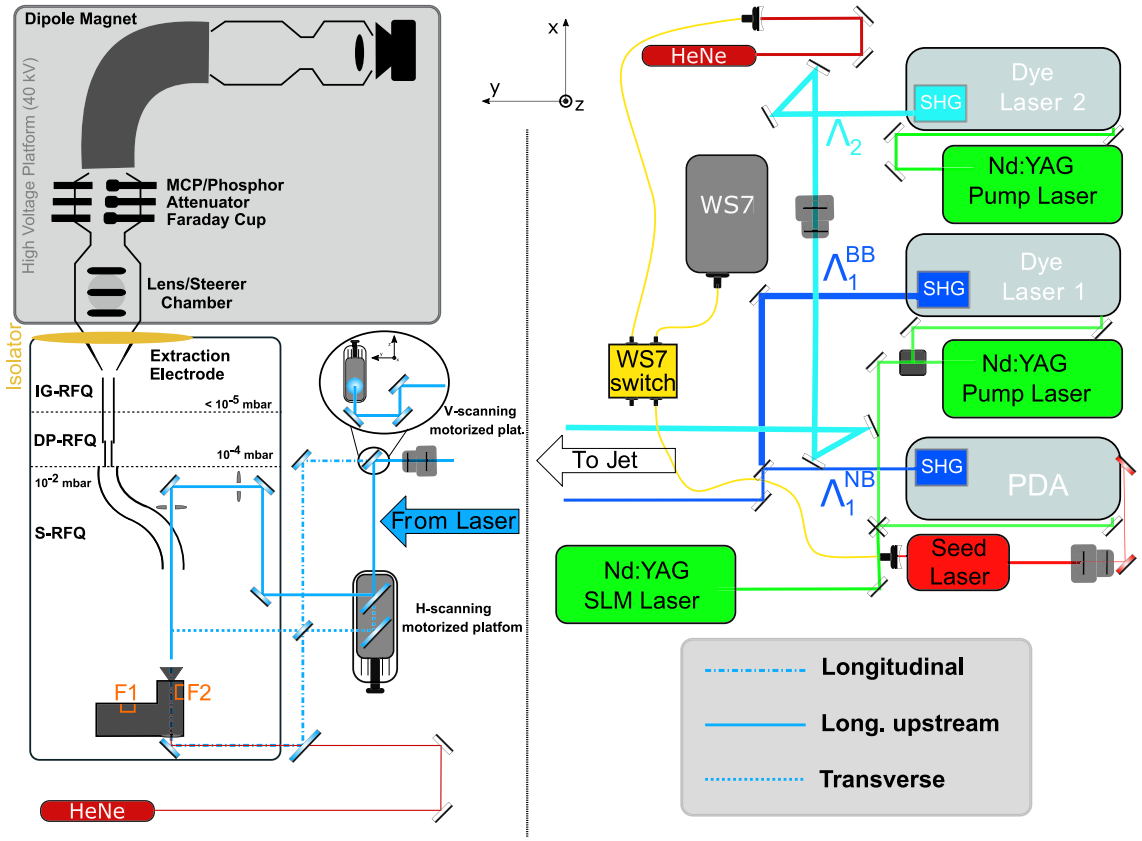

FIG. 4. Schematic layout of the IGLIS laboratory (see text for details). The required laser radiation is produced by a Nd:YAG pumped dye-laser system with integrated frequency conversion units and guided to the gas-jet beam line located in a separate room. The laser beams can be arranged in different beam paths corresponding to various interaction geometries in the gas cell/gas jet. Specific paths for each laser define the region of overlap where atoms are ionized.

further excites the atoms above the ionization potential to an autoionizing state at 65260.1 cm^{-1} with a typical laser power of 2 W. In this way, the consecutive action of the broad or narrow bandwidth Λ_1 with Λ_2 results in the resonance ionization of copper atoms in a distinct region of the jet where the laser beams overlap in space. The wavelength of all lasers can be monitored by a wavelength meter (WS7, HighFinesse GmbH) regularly calibrated by a frequency-stabilized helium-neon (HeNe) laser [23,24].

The obtained photo-ions are then confined and transported by a set of radio-frequency quadrupole (RFQ) ion guides comprising an S-shape RFQ (S-RFQ), a small differential pumping RFQ (DP-RFQ) and a long ion-guide RFQ (IG-RFQ). These ion guides enable the transport of ions through different pressure regions up to a high-vacuum section, where they are accelerated to an energy of 40 keV. Notice that owing to the low electric fields applied to the first segments of the S-RFQ (0 V DC and 350 V_{pp}, i.e., ±175 V, at 1 MHz radio-frequency field) we can consider the jet volume a field-free region. Next, the ion beam is electrostatically focused and guided towards a dipole magnet where the two stable copper isotopes ^{63,65}Cu, in a singly-ionized charge state, can be selected according to their mass-to-charge ratio with a usual resolving power of $R = m/\Delta m = 325(25)$. The ion arrival can finally be recorded at the focal plane of the dipole magnet either by a Faraday cup or a multichannel plate (MCP) detector.

With the help of a set of laser mirrors placed on motorized platforms (see Fig. 4) we can vary, in a reproducible manner, the intersection volume of the Λ_1 and Λ_2 beams along the horizontal and vertical dimensions of the jet. In this way, we are able to obtain a full mapping of the flow properties by scanning the frequency of the narrow-band Λ_1^{NB} around the 327 nm transition, while keeping a fixed frequency in Λ_2 and recording the ion counts in the MCP detector. This resonance ionization process makes it possible to probe the hyperfine structure of the $^2S_{1/2}$ to the $^2P_{1/2}$ transition in the copper atoms, such as done with fluorescence photons in the PLIFS method. Unlike the latter, the RIS mapping method, however, provides mono-isotopic samples making the analysis of the resulting spectra easier. Both lasers can be aligned to any beam path to offer ultimate flexibility. Simulated RIS scans of two jet zones at different temperatures are shown as an example in Fig. 5. From such scans information on the local velocity, temperature and relative density of the jet can be inferred by analysis of the Doppler shift, width, and amplitude, respectively, of the scanned hyperfine transi.

The transport efficiency of copper ions using the hypersonic nozzle and a longitudinal excitation and ionization laser geometry in the gas cell has consistently been measured to be 55(5)% up to the first Faraday cup (FC1) located before the dipole magnet (see Fig. 4). This is a significant reduction in comparison to previous experiments using a different nozzle, in which we reported an average transport efficiency of

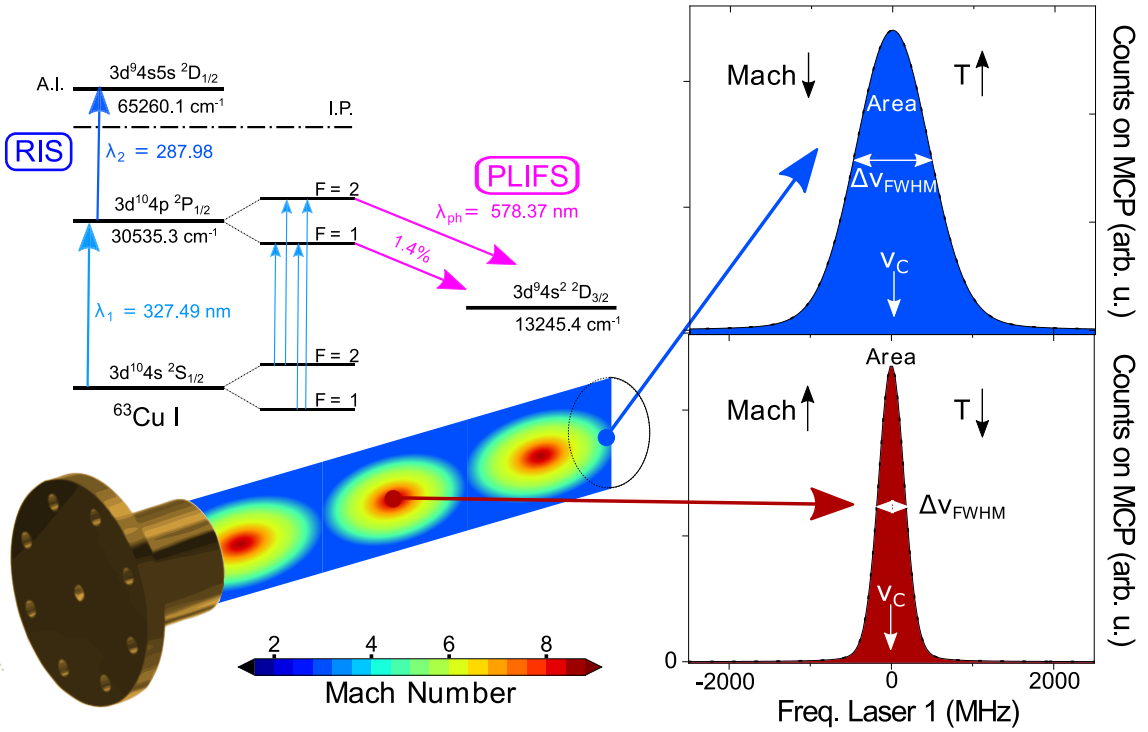

FIG. 5. Schematic overview of the RIS mapping method in a laser geometry mapping the central line (core) of the jet. The copper atoms are ionized via an auto-ionizing state (A.I.) in a two-step scheme shown in the upper-left corner. The de-excitation to the metastable state at $\lambda_{ph} = 578$ nm used in the PLIFS measurements is also indicated for the sake of completeness. All wavelengths are given in vacuum. The Mach number of the probed region determines the spectral characteristics of the hyperfine spectrum. These observables can then be used to obtain the local flow parameters (see text for details).

91(7)% [13]. The main cause for the current lower efficiency is the extremely long and well-collimated jet produced by the hypersonic nozzle that extends for more than 190 mm. This improved jet collimation and uniformity, in comparison to the jets produced by other previously tested nozzles, increases the momentum transfer of argon to the copper ions, resulting in more unfavorable conditions for the copper ions to be confined in the pseudopotential of the S-RFQ ion guide. For the typical pressure of a well-formed jet a copper atom undergoes about 10 collisions per μs, that is to say per one cycle of the oscillating RF in the S-RFQ driven at 1 MHz. Owing to the high uniformity and collimation of the jet these collisions result in an effective force in the forward direction. In fact, in order to minimize such an effect and thus the amount of ions flying through the first bend in the S-RFQ, we had to increase the distance from the nozzle to the entrance of the S-RFQ up to 190 mm, the maximum allowed by the dimensions of the gas cell chamber. Only in this way, a maximal transport efficiency of the ions up to FC1 could be obtained. Further developments in the ion guides are being considered to improve the overall ion transport efficiency.

Furthermore, the ionization efficiency in the gas cell and the gas jet was directly compared using a transverse excitation and ionization laser geometry in the former and a transverse excitation and a longitudinal-upstream ionization laser geometry in the latter. In order to increase the duty cycle of laser irradiation of isotopes seeded in the gas jet, a key indicator to maximize the ionization efficiency in online experiments, the beam of the excitation step laser Λ_1^{NB} was shaped into a sheet that had the expected gas jet core dimension in the vertical direction, whereas the horizontal length was matched with the laser at 10-kHz repetition rate, such that each atom interacted at least once with a laser pulse. The ionization laser Λ_2 subsequently covered the full gas jet core region with an estimated average diameter of 4 mm. The results showed that only 70(10)% of the atoms ionized in the gas cell could be ionized in the gas jet with the main problem being the available laser power to saturate the ionization step in the gas jet. A careful examination of the saturation conditions of both excitation and ionization steps in the gas-cell and gas-jet environments revealed a fair saturation level for both transitions in the former and a deficient power density level in the latter, which became more severe in the case of the ionization step. A simulation of the broadband laser interaction with copper atoms in both cell and jet conditions, using the laser atom interaction code from [25], allowed for a model-dependent extrapolation of the data [26]. These results indicate an increase in efficiency with a factor 16(8), which is in agreement with the experimental extrapolated ionization efficiency for the actinium isotopes in the gas jet reported in Ref. [8].

In the RIS scans we ionize both stable copper isotopes with a natural abundance of 69.15(15)% to 30.85(15)% for ^{63}Cu and ^{65}Cu, respectively, and only detect ^{63}Cu in the focal plane of the dipole magnet, which also has 80(5)% measured transmission efficiency. Owing to the nonoptimal cleanliness conditions of the apparatus in the course of these characterizations studies about 50% of the ^{63}Cu ions were lost by the for-

mation of the water adducts $^{63}Cu[H_2O]^+$ and $^{63}Cu[2H_2O]^+$. Taking this into account, an overall efficiency of the RIS mapping method of $\epsilon_{tot} = \epsilon_{trans} \times \epsilon_{abund.} \times \epsilon_{magn.} \times \epsilon_{adduct} = 0.55(5) \times 0.6915(15) \times 0.80(5) \times 0.50(10) = 15(3)\%$ can be concluded from these measurement, disregarding the ionization efficiency and any geometrical efficiency associated with the spatial overlap of the laser beams with the jet. This efficiency is about 75 times better than that obtained under similar grounds in the PLIFS measurements. It has been shown that a dedicated bake out of the gas cell, the gas supply lines and a thorough vacuum testing after these measurements could practically remove all the water adducts [26].

IV. RESULTS

A. PLIF measurements

In a first series of studies we performed relative flow-density measurements using the PLIF method. These measurements proceeded in the same way as described in detail in Ref. [14]. Copper isotopes produced in the gas cell were extracted through the nozzle along with argon as the carrier gas. The broad bandwidth output of Λ_1^{BB} (see Fig. 4) at a wavelength of 327.49 nm was sent to the gas jet in transverse geometry to excite the copper atoms from the $^2S_{1/2}$ ground state to the $^2P_{1/2}$ excited state with a lifetime $\tau = 7.2$ ns. Following such an excitation scheme, a small branching of 1.4% of the atoms de-excite to the metastable $^2D_{3/2}$ state emitting a photon at $\lambda_{ph} = 578.37$ nm (cf. ionization scheme in Fig. 5) that was recorded by a high-resolution, wide dynamic range intensified CCD camera. The magnitude of the branching ratio is an important factor in the low efficiency of the PLIF method.

A set of pictures, comprising each 600 camera acquisitions, were performed at different background pressures P_{bg} to visualize the resulting gas jet. A single acquisition was the result of triggering the camera with each laser pulse to open the photocathode by 50 ns for a total exposition time of 1 s. Thus, at 10 kHz pulse repetition rate, a picture is the accumulation of 600 times 10 000 collections of 50 ns each. The left panel in Fig. 6 shows a selection of the data illustrating the flow evolution from overexpansion (top pictures) to underexpansion (bottom pictures) crossing the matched flow condition, for which the background pressure and the pressure at the nozzle exit are similar, that is $P_e \sim P_{bg}$. For a matched flow, indicated by the green-framed picture, one obtains a quasiparallel and highly uniform gas jet. This uniformity is evident in the corresponding density profiles shown in the right panel of Fig. 6, which result from the evaluation of the relative flow density with respect to the average value, for a stagnation pressure $P_0 \sim 300$ mbar and a stagnation temperature $T_0 \sim 490$ K (see end Sec.IV). For the matched flow, i.e., when $P_{bg} = 0.10$ mbar, a relative density variation of only 3% is observed over a distance of 25 mm and the ratio $P_0/P_{bg} = 2960$ can be used to obtain a rough estimate of the Mach number $M = 8.4(3)$, with the error bar being defined by the dispersion of the Mach number values obtained for the closest background pressures to the optimal one. This value for the average flow Mach number is in line with the results from a new set of CFD simulations performed at the aforementioned stagnation conditions. The relative density profiles

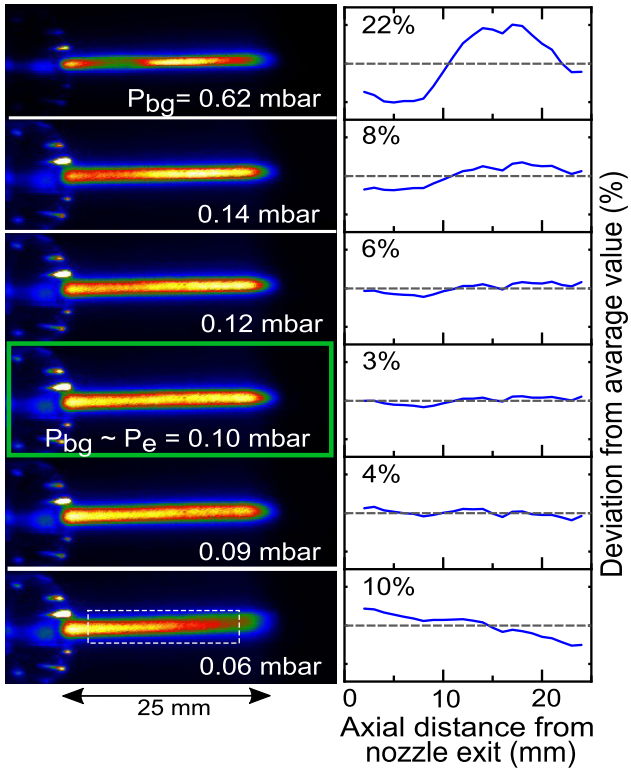

FIG. 6. (Left panel) Visualization of the relative gas-jet density for $P_0 = 300$ mbar and $T_0 \sim 490$ K at different background pressures P_{bg}. The color code indicates the fluorescence intensity with black (lowest) to white (highest) relative scale in each picture. The green rectangle indicates the P_{bg} that results in a matched flow, i.e., $P_{bg} \approx P_e$. (Right panel) Variation of the relative gas-jet density with respect to the average value (dashed line) obtained from the integrated intensity of the pixel area, indicated with a dash-lined rectangle, for the jets shown on the left.

show the sensitivity of the jet uniformity to small variations of P_{bg}, as anticipated by the CFD simulations.

B. RIS Measurements with PLIFS verification

Using the matched flow conditions found in the PLIF measurements we proceeded with the characterization of the local velocity and temperature along the central line (core) of the jet by means of the RIS method. The output radiation of either the single-mode Nd:YAG pumped PDA or the multimode Nd:YAG pumped PDA, was overlapped in a longitudinal-upstream geometry, covering a region larger than the expected gas-jet size, while Λ_2, having a laser beam diameter of <1 mm, scanned transversally the jet in the horizontal and vertical planes with the help of two mirrors mounted on motorized platforms [see Fig. 7(a)]. The jet axis was mapped by taking measurements along a total distance of 96 mm in steps of 4 mm. To make sure the center of the jet was intersected, the vertical dimension was scanned for each point to obtain the maximum count rate at which the hyperfine spectrum was taken. For each position of Λ_2, Λ_1^{NB} was detuned slightly below the central wavelength at 327.49 nm to probe the two lower energy hyperfine transitions ($F = 2 \rightarrow 1$ and $F = 2 \rightarrow 2$) in ^{63}Cu produced by filament

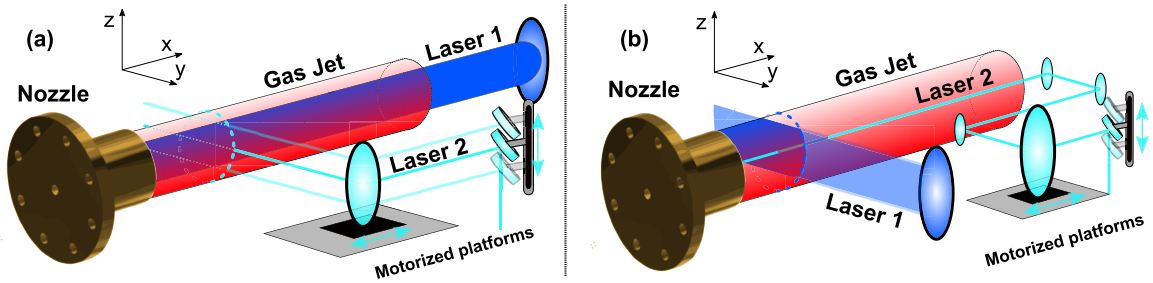

FIG. 7. 3D impression of two laser-path geometries, described in the text. The gas jet, Laser 1 and Laser 2 are schematically shown in red, dark blue, and light blue, respectively. (a) Beam paths used to carry out the mapping of the central line in the gas jet. The narrow-band Λ_1^{NB} in a longitudinal-upstream geometry and Λ_2 probing the jet in perpendicular planes with the use of the motorized mirrors. (b) The arrangement used to study the cross sectional density plots reported in Fig. 11. Here, the broadband Λ_1^{BB} excites a sheet of atoms in the gas jet, with only those ionized where Λ_2 intersects with the sheet.

F2. A typical mapping of the jet central line consists of 25 ionization scanned zones with each of the scans comprising 40 excitation frequency steps and five accumulations of 1 s per step, which resulted in a total time of ≈80 minutes. The five accumulations were taken to offer a better estimate of the true count rate and its uncertainty. In case time is of the essence, less accumulations can be performed without a strong increase in the uncertainty of the fit parameters. As an example, the left panel of Fig. 8(a) illustrates the result of one of such scans taken at 17 mm from the nozzle exit. The spectra were fitted using a χ^2 minimization of a double-peak Voigt (i.e., a convolution of a Gaussian and a Lorentzian) profile to obtain the centroids (ν_C) and full width at half maximum ($\Delta\nu_{\mathrm{FWHM}}$) of the peaks. T and T_0 alone define these observables and therefore are the only fit parameters in the model. Other parameters, such as the pulse length of the laser, were measured in separate experiments. In case the multimode Nd:YAG pumped PDA was used, the spectral sidebands [12] were taken into account as described in Ref. [26]. The centroid dependence on T and T_0 can be written as follows:

$$\Delta\nu_C = (-1)^{\beta}\frac{\sqrt{\frac{2\gamma k_b(T_0-T)}{m_1(\gamma-1)}}}{\lambda_{\mathrm{vac}}\times 10^6}, \tag{1}$$

with γ the ratio of specific heats $C_p/C_v = 1.67$ for monatomic (e.g., noble) gases, m_1 the mass in kg of an argon atom, λ_{vac} the wavelength in nm of the reference obtained in vacuum conditions and $(-1)^{\beta}$ with $\beta = 0$ or 1 for a longitudinal-upstream or -downstream overlap, respectively, of the probe laser with the gas jet axis. The Lorentzian contribution to the $\Delta\nu_{\mathrm{FWHM}}$ is defined as follows:

$$\Delta\nu_{\mathrm{FWHM,L}} = \Delta\nu_{L,\mathrm{Col}} + \Delta\nu_{L,\mathrm{Nat}}, \tag{2}$$

with

$$\Delta\nu_{L,\mathrm{Col}} = \frac{T^{1/(\gamma-1)+0.3}\gamma_{\mathrm{Col}}P_0\times 10^{-4}}{T_{\mathrm{room}}^{0.3}T_0^{\gamma/(\gamma-1)}k_b}, \tag{3}$$

$$\Delta\nu_{L,\mathrm{Nat}} = \frac{A_{\mathrm{Ein}}}{2\pi}, \tag{4}$$

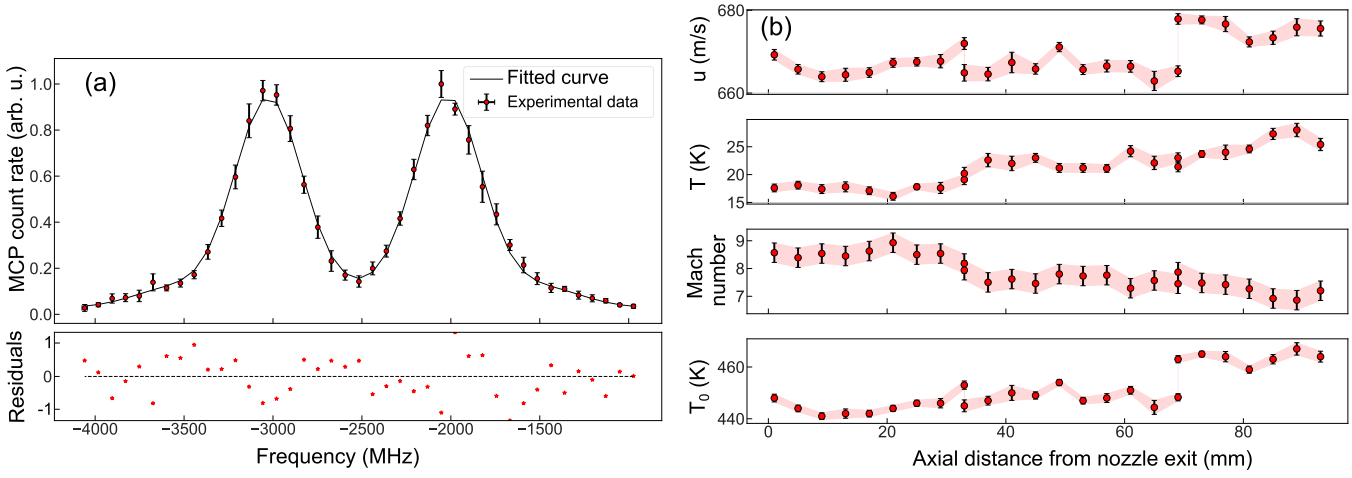

FIG. 8. (a) Partial hyperfine structure of the 327.49 nm transition in ^{63}Cu showing the lower energy transitions (see level scheme in Fig. 5) obtained by the RIS mapping method. The solid line is a Voigt fit to the data points. The frequency is shown as the detuning with respect to the $F = 2 \rightarrow 2$ hyperfine transitions in ^{63}Cu measured in vacuum at $\lambda = 327.4919$ nm. The residuals of the fit are shown below. (b) Local flow velocity u and temperature T of the gas jet determined from the fitted parameters and the computed Mach number M and stagnation temperature T_0. The data was collected in two consecutive measurements interrupted by the time elapsed to change the position of the entrance 2-inch UV windows in the gas cell chamber. The offset observed in the central part might be explained by a slight change of T_0 between the two measurements.

being the parts corresponding to the collisional and natural linewidths, respectively.

In these equations, P_0 is the stagnation pressure in the gas cell (mbar), A_{Ein} (MHz) represents the Einstein A parameter of the transition, k_b is the Boltzmann constant, $T_{\mathrm{room}} = 300$ K and $\gamma_{\mathrm{Col}} = 6.2(8) \times 10^{-16}\mathrm{MHz/cm^{-3}}$ is the collisional broadening factor [26]. The contribution of the ionization laser to the $\Delta\nu_{\mathrm{FWHM}}$ was evaluated by reference scans taken during the measurements, with delayed laser pulses [25]. To eliminate the contribution of parts of the jet outside the central core region a correction of the initial laser beam geometry was done by acquiring data with a decreased beam size of Λ_1^{NB}, aimed through an optical path delimited by the nozzle throat and a 1-mm-pinhole installed in the gas cell view port opposite to the nozzle (see Fig. 4). The power broadening originating from the the PDA output used for excitation was minimized before each measurement run by defining the beam intensity from which the $\Delta\nu_{\mathrm{FWHM}}$ remained constant while lowering the laser intensity. The Gaussian contribution to the FHWM can be written as

$$\Delta\nu_{\mathrm{FWHM,G}} = \sqrt{\Delta\nu_{G,\mathrm{Dop}}^2 + \Delta\nu_{G,\mathrm{L}}^2}, \tag{5}$$

with

$$\Delta\nu_{G,\mathrm{Dop}} = 7.16 \times 10^{-7}\nu_0\sqrt{\frac{T}{A}}, \tag{6}$$

$$\Delta\nu_{G,\mathrm{L}} = \frac{441}{\Delta\tau_L}, \tag{7}$$

being, respectively, the parts accounting for the Doppler broadening and the laser bandwidth.

Here, ν_0 represents the resonance frequency (MHz), A is the atomic mass number of the seeded (copper) atoms, and $\Delta\tau_L$ is the half-width duration of the excitation laser pulse (ns), assuming that the PDA laser pulse is Fourier limited.

The model, finally, fits the best combination of T and T_0 to the data, see Fig. 8(a) for an example. This fit makes it possible to deduce the flow velocity and flow temperature in each point and compute the evolution of the flow Mach number along the jet [see Fig. 8(b)].

In Ref. [14], we applied the PLIFS method to obtain the flow properties of a jet in free expansion and could, in this way, verify the validity of the method by comparing the experimental results with the well-known analytical solutions. Following a similar reasoning, in these studies we performed PLIFS measurements under matched flow conditions in order to realize a direct comparison of both, the RIS and PLIFS, methods that could serve to verify the validity of the results obtained by the former. In these measurements the output of Λ_1^{NB}, this time achieved by the multimode Nd:YAG laser pumping the PDA, was overlapped in a longitudinal geometry with the central line of the gas jet. About 50 frequency steps were taken, each of them comprising 50 camera acquisitions with the same characteristics (i.e., 50 s per frequency step) as those used in the PLIF measurement. On the top panel of Fig. 9 a typical image obtained in these measurements is shown, which corresponds to the resonance frequency of the hyperfine component $F = 1 \rightarrow 2$ in ^{63}Cu and, with a much smaller contribution, of $F = 1 \rightarrow 1$ in ^{65}Cu. Notice that no

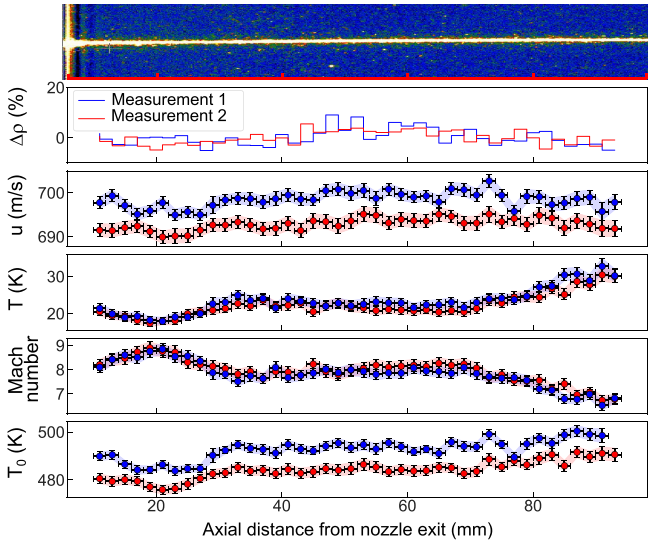

FIG. 9. As in Fig. 8, the results for the local flow properties such as velocity u, jet temperature T, as well as the deduced Mach number M, and stagnation temperature T_0 obtained in two consecutive PLIFS measurements are presented. A typical PLIF image used in these measurements to extract the data is shown in the top panel.

mass separation of the two stable copper isotopes is possible in the PLIFS measurements. The picture shows a fairly uniform jet, indicating a good collimation such as those shown in Fig. 6, extending for a distance of ≈100 mm. A pixel analysis of similar pictures recorded at 50 laser frequency steps around the high energy hyperfine components of the 327.49 nm transition could then be used to obtain the local velocity and temperature of the gas jet in a similar fashion as with the RIS data. The results corresponding to the measured velocity u an temperature T as well as to the deduced Mach number M and stagnation temperature T_0 are shown in Fig. 9 for two consecutive scans. Unlike in the RIS method, the completion of the PLIFS scans took a longer time, which made it difficult to keep steady stagnation conditions such as T_0 and P_0. In spite of that, we can see from the results that different initial stagnation temperatures T_0 (a difference of about 10 K in average was observed between the two measurements) do not have a significant repercussion in the final average Mach number of the jet. Notice that owing to the intrinsic low efficiency of the applied PLIFS method using copper in the IGLIS laboratory, filament F2 had to be implemented additionally in the gas cell design. Apart from being closer to the gas cell exit, which minimizes transport losses within the cell, the fact that F2 is installed in the narrow exit channel with better cooling (heat exchange) conditions, enables the production of a higher density copper vapor in comparison to F1. The use of F2 is therefore essential to perform PLIFS studies, but is not the case when applying RIS mapping, as the sensitivity of the method can easily cope with the lower copper production by F1. Because of the longer transit time, the buffer gas heated by F1 can be efficiently cooled before reaching the exit hole, enabling in-gas-jet laser spectroscopy measurements at T_0 close to room temperature. Figure 10 summarizes the results extracted for the evolution of the lo-

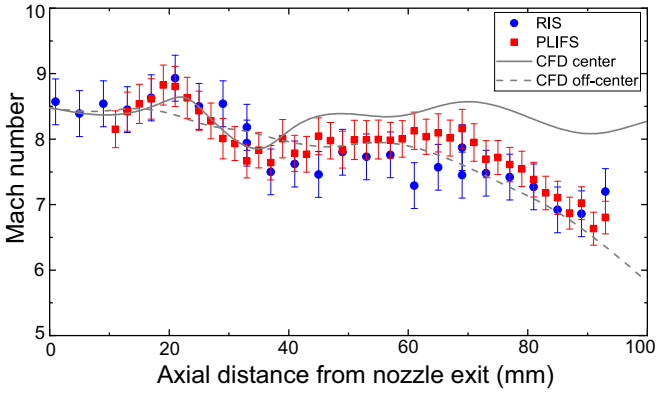

FIG. 10. Evolution of the Mach number as a function of the distance from the nozzle exit obtained by the RIS (blue dots) and PLIFS (red squares) methods using filament F2, as well as the CFD prediction when considering a perfect (solid line) and a slightly tilted (dashed line) overlap of the laser beam with the central axis of the gas jet.

cal flow Mach number by the RIS mapping and the PLIFS methods as well as that obtained by numerical CFD simulations at stagnation conditions $P_0 = 300$ mbar and $T_0 = 450$ K. The uncertainties corresponding to the RIS measurements are a combination of the fitting results and the applied corrections discussed above, which could be both greatly reduced in future measurements. The PLIFS error bars comprise statistical fitting uncertainties and a systematic uncertainty related to the unresolved sidebands. Looking first at the experimental results it becomes clear that the new RIS method and the PLIFS method agree very well in their description of the gas jet. Only in the central part of the scan, from a distance of about 35 to 70 mm from the nozzle exit, a systematic offset between the two data set is observed. Owing to the availability of only 2-inch diameter UV coated windows in the vacuum chamber, the data corresponding to the central part was taken after a short rearrangement of the windows. The elapsed time to install the new window geometry might well have induced a slight change in the gas cell temperature, and thus in T_0, or some sort of optical misalignment of the laser with respect to the jet, suggested by the two data points on the extremes, which show a similar offset with respect to the last and first points of the precedent and following scanned parts.

On the other hand, Fig. 10 also reveals an excellent agreement of the CFD predictions for the Mach number in the central line (solid line) with those obtained experimentally up to a distance of ∼70 mm from the nozzle exit. From this point on, the experimental data is consistent with a gradual decrease of M while increasing the distance from the nozzle exit. This sudden decrease is not yet well understood but could be explained by a mechanical (in contrast to an optical) misalignment of the laser in a longitudinal geometry with respect to the central axis of the jet. This situation is illustrated in Fig. 10 by the dashed line obtained when the results of CFD calculations consider such a misalignment to be of 1°. Despite the nozzle being machined with a high accuracy, mechanical imperfections in the gas cell platform, in the wall of the gas cell in which the nozzle rests, or even in the sealing gasket in between those two, could induce such a deviation.

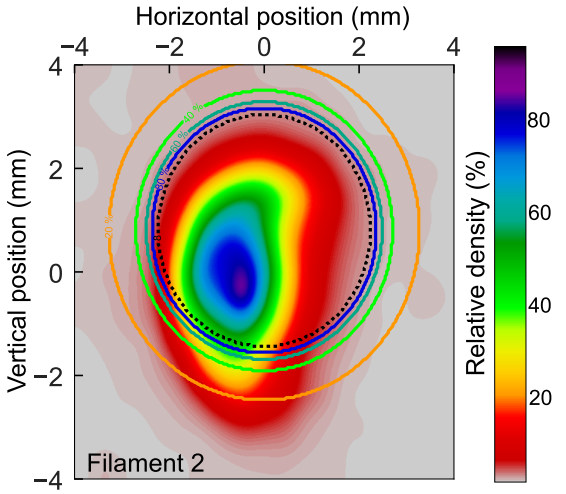

FIG. 11. Cross-sectional view of the copper density seeding the argon gas jet by the RIS mapping method when filament F2 is used. The image was obtained employing the laser alignment illustrated in Fig. 7(b), normalized to the maximum pixel count rate. Additional contour lines are added, corresponding to the simulated argon density from Fig. 2 (solid lines). The color of these lines shares the same scale as the color bar on the right and, thus, also as the experimental results. The dotted line represents the Mach 8 contour line indicating the limiting dimensions of the central core region of the jet with nearly homogeneous Mach number. The coordinate axes are referenced relative to the position of the motorized platforms.

Another reason for the observed discrepancy between the CFD simulations and the experimental results could lie in the nonequivalence between seeded atoms and buffer gas by which the copper atoms would traverse the expanding flow not necessarily coinciding with the core of the argon jet. Arguments in favor were found in PLIFS measurements of the expanding free jet reported in Ref. [14]. Taking advantage of the flexibility offered by the RIS mapping method to examine the flow in any geometrical plane, we performed a series of measurements to study the relative density of copper in the y-z plane, perpendicular to the direction of flow propagation [cf. Fig. 7(b)], when the copper atoms were produced at different locations within the gas cell, namely by filaments F1 or F2 (see Fig. 4), and evacuated through the nozzle. The output of Λ_1^{BB}, shaped as a thin vertical sheet, interacted in transverse geometry with the gas jet at a distance of 1.5 cm from the nozzle exit, while Λ_2 in a longitudinal-upstream geometry mapped the radial plane of the jet by intersecting Λ_1^{BB} in a cross-section of approximately 2D pixels. The results for the relative density distribution of copper in the argon flow when the former was produced by filament F2 is shown in Fig. 11 along with a simulated profile from the data of Sec. II in the form of contour lines denoting the predicted relative density with respect to the core region. The approximate location of the center of the gas jet was located by laser alignment through an iris installed in the view port opposite to the gas-cell exit hole and concentric with it. The obtained density profiles did not match the predicted jet shape and showed an asymmetry with respect to the jet center. Because of the observed poor ion-transport efficiency through the S-RFQ when using F1 in these measurements (see below) we opt here for focusing

the discussion on only filament F2. The atoms from filament F2, which is located near one of the walls (the left one in the view direction) of the gas cell exit channel (total transit time ≈5 ms), clearly show an asymmetric density distribution shifted sidewards, in correspondence with the filament position. These results are also in agreement with the sidewards displacement of the copper concentration obtained also by PLIF images [27]. Therefore, the results presented in Fig. 10, using F2, do indeed provide the Mach number of the central core, as the lasers were aligned to the center of the copper distribution, vertically, which for this filament corresponds to the center of the jet. A confirmation of the results shown in Fig. 10 was found by measurements in which Λ_1^{NB} was carefully aligned in a longitudinal geometry, limited in size by the 1-mm exit hole.

On the whole, we can state that copper does not necessarily mimic the dimensions and density distribution of the argon gas jet, as would be expected with realistic diffusion coefficients. The position of copper in the jet, however, shows a dependence on the location within the gas cell where it was produced. The laser arrangement discussed here can be used in the future to perform a full 3D mapping of the gas jet by collecting data as in Fig. 11 and as a function of laser wavelength. In such a way, the dimensions of the argon jet could be extracted from the obtained Mach number distribution along the jet symmetry axis and from the radial cross sections.

As a matter of fact, the confinement of ions by the S-RFQ, and hence the total transmission efficiency up to the ion detector located at the focal plane of the mass separator, also shows a dependence on the distribution of copper atoms in the jet. When copper is produced by F1, additional deflectors installed at the entrance of the S-RFQ have to be used to push the ions inwards so that a more compact ion distribution is obtained, as that resulting from F2, and a maximal transmission efficiency can be achieved.

This asymmetry in the relative density distribution of copper triggered a new set of measurements of the flow properties using filament F1. We performed a number of RIS measurements along the central line of the jet at different positions from the nozzle exit operated under matched flow conditions, as those reported earlier in the text, but now also using F1. A clear difference when performing RIS with filaments F1 or F2 was evident in the results obtained for the flow velocity u. As we saw in the PLIFS measurements presented in Fig. 9, small variations in the stagnation temperature T_0 are reflected in the resulting flow velocity. For F1 the flow velocity was found to be around $u = 560$ m/s, which corresponds to a stagnation temperature $T_0 = 315$ K close to room temperature, in contrast to the $T_0 \sim 450$–490 K extracted when using F2. The increase in T_0 when using F2 is understood as more power is applied to this filament, which is much closer to the gas cell exit, that translates in less time for the heated gas surrounding the filament to get thermalized by collision with other atoms before exiting the cell. This is in contrast with those atoms surrounding F1, which undergo significantly longer extraction times. The results for the Mach number determination in stagnation conditions given by filaments F1 and F2 are shown in Fig. 12. In view of these results, a question lingered as to why working at room temperature deteriorated the nozzle performance.

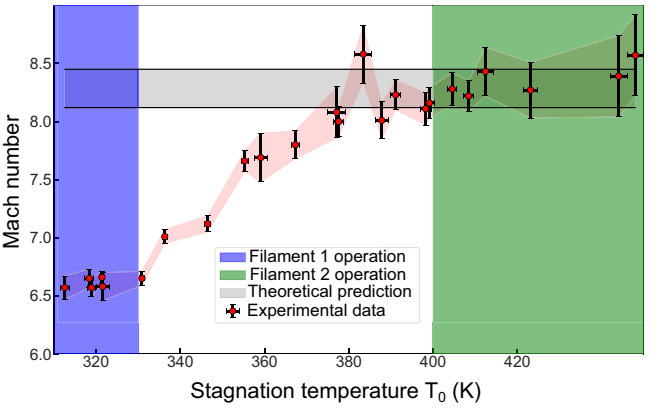

FIG. 12. Mach number dependence on stagnation temperature T_0. The experimental points are obtained as discussed in the text. As increasing T_0 means slightly also increasing P_0, such an influence is accounted for in the expected theoretical prediction band, which is based on adiabatic and isentropic expansion through the nozzle. In theory, a decrease of stagnation temperature should be followed by a decrease in jet temperature to keep the Mach number constant. The working regions for filaments F1 and F2 are also indicated.

V. MACH NUMBER DEPENDENCE ON STAGNATION TEMPERATURE: ONSET OF ARGON NUCLEATION

The RIS method was finally applied to study the dependence of the Mach number M on the stagnation temperature T_0. One should keep in mind that T_0 is deduced from the Doppler shift of the resonance centroids of the probed hyperfine transition in copper. Prior to these measurements we exchanged the copper filament in position 2 by a molybdenum filament with an identical geometry. In this way we decoupled the production of copper by F1, operated at a constant power, from the action of F2 used as heating source to increase T_0. We operated F1 at the minimal power conditions to perform RIS, at a distance of about 5 mm from the nozzle exit, on the resulting gas jet under matched flow conditions. While keeping constant the power applied to F1, we then started to power F2, which we varied gradually in each consecutive measurement, so that to increase T_0. The results obtained for the evolution of the Mach number M and the jet temperature T as a function of the stagnation temperature T_0 are shown, respectively, in Figs. 12 and 13(a).

This behavior of M is surprising as it departs from the linear trend expected from an isentropic expansion of a compressible flow, indicated in the figures by the shaded area between lines. The nozzle free-stream Mach number is fixed in theory by the nozzle geometry, as previously described. Although slight variations from the designed value can be expected when the nozzle boundary layer displacement thickness δ^* varies, that is, when the local Reynolds number Re is modified, these changes in Mach number, however, would require significant variations, in comparison to what here is shown, of the stagnation pressure and temperature. As the Mach number is defined by the ratio of T and T_0 such that

$$\frac{T}{T_0} = \left[1 + \left(\frac{\gamma - 1}{2}\right) M^2\right]^{-1}, \tag{8}$$

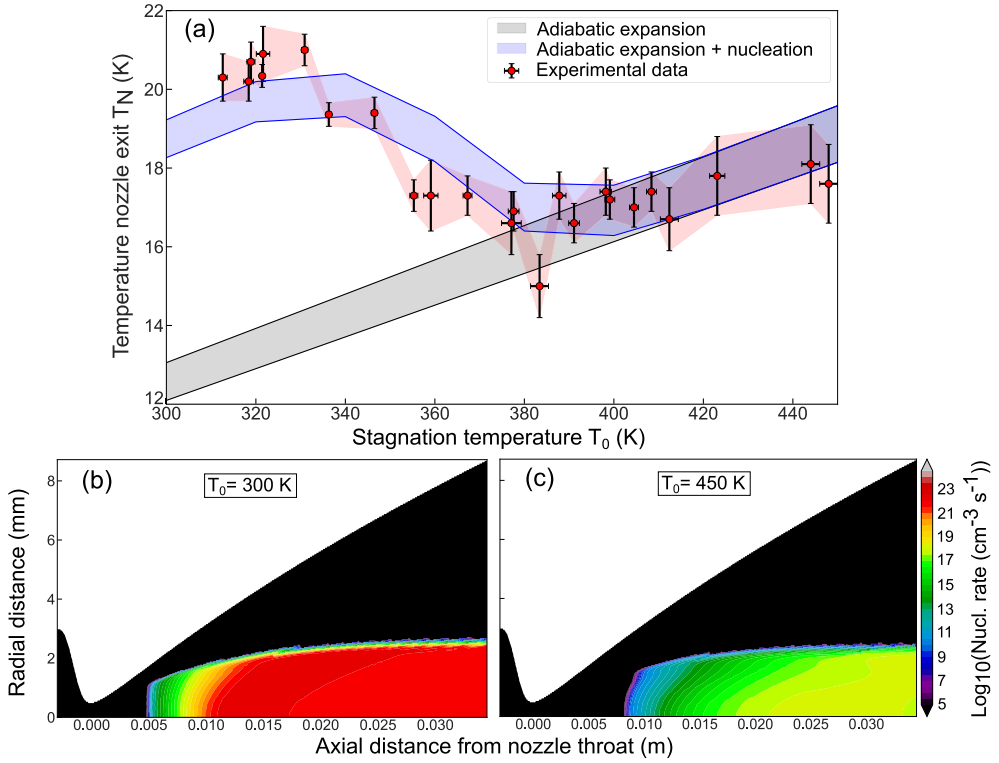

FIG. 13. (a) Experimental data points and calculated isentropic/adiabatic expansion predicting T (gray shaded area), supplemented with the nucleation simulations discussed, presenting T_N. One can see that the simulations predict the onset of nucleation in the jet temperature measurements to high accuracy. [(b),(c)] Showing $J_{\text{MKNT-XS}}$ as a function of the hypersonic nozzle dimensions with $X = 0$ defined at the nozzle throat, for $T_0 = 300$ K (left) and $T_0 = 450$ K (right). All points where $J_{\text{MKNT-XS}} < 1\,\text{cm}^{-3}\,\text{s}^{-1}$ are omitted. Also here, it becomes evident that different stagnation temperatures have a significant influence on the total integrated nucleation rate.

a larger stagnation temperature T_0 in the experiment should be compensated by an increase in jet temperature T to keep the Mach number M constant. However, in the results of Fig. 12 the opposite is observed, explaining the decrease in the computed Mach number. The argument that this behavior cannot be explained by the normal adiabatic and isentropic expansion of the gas through the de Laval nozzle, was confirmed by a new set of CFD simulations, which revealed no significant difference in the flow parameters calculated for $T_0 = 300$ K and $T_0 = 450$ K. One may also notice that since the local Reynolds number at the nozzle exit is defined as $Re = \rho u L/\mu$, with ρ being the gas density, u the flow velocity, L the running length along the nozzle contour, and μ the flow viscosity, an increase of density by increasing P_0 or, to a lesser degree, decreasing T_0, will be associated with an increase of Re. This would correspond to a reduced local boundary layer thickness, as the boundary layer displacement thickness $\delta^*(x)/x \propto 1/\sqrt{Re}$, where x is the axial distance measured from the nozzle throat. Consequently, one could design a nozzle with a higher Mach number for operation at a higher stagnation pressure, or a smaller viscous correction on the inviscid nozzle contour would be required to get the same nozzle exit Mach number. In any case, the observed Mach number (jet temperature) trend in Fig. 12 [Fig. 13(a)] with decreasing the stagnation temperature T_0 is opposite to what one could expect from a Reynolds number effect.

A plausible explanation for the observed phenomenon lies in the process of argon nucleation, whereby the temperature and pressure conditions become such that the gaseous phase develops into a metastable state of the system tending to evolve into the liquid phase, thus releasing energy in the process and increasing the overall temperature [28,29,29]. Examination of the results in the literature for the conditions of the onset of nucleation and the flow parameters T and P expected in the expansion of the gas through the hypersonic nozzle studied here, reveals that a significant degree of nucleation might occur and could, therefore, be considered in this discussion. The fact that a lower T_0 results on average in lower temperatures during gas expansion, could trigger a significant process of nucleation and, hence, a local increase in the jet temperature T. This matches qualitatively with the trend observed from experimental results.

To provide also a quantitative comparison with the experimentally observed temperature at the nozzle exit, the nucleation rates, calculated as a function of the flow parameters within the nozzle, should be converted to a total temperature increase due to nucleation (see Appendix).

A. Nucleation rate calculations and results

The nucleation rate at each point $\vec{z}$ of the nozzle is a function of the temperature $T(\vec{z})$ and pressure $P(\vec{z})$: $J(\vec{z})) = J[T(\vec{z}), P(\vec{z})]$. In the present study the simulated flow parameters (T, P) along the nozzle obtained in the absence of nucleation are used as the input for the nucleation rate studies. Our experimental conditions correspond to high values of the

supersaturation S characterizing the degree of metastability of the vapor phase: $30 < \ln S < 50$. These conditions correspond to extremely small (molecular-sized) critical clusters. Classical nucleation theory (CNT), which has long been the most widely used theoretical model, fails to predict nucleation rates in the situations when small, molecular-sized, clusters play the leading role in the system behavior. This shortcoming gave rise to a number of efforts aimed at understanding nucleation at the molecular level, which requires taking into account of intermolecular interactions. One of such models is the mean-field kinetic nucleation theory (MKNT) [30] (see also [28], Ch. 7), which treats small clusters using statistical mechanical considerations and provides a smooth interpolation to the limit of big clusters obeying the classical CNT description.

A special feature of the hypersonic flow produced by the nozzle characterized in these studies is that some parts of it correspond to extremely high S, falling into the so-called *XS-domain* of temperatures and supersaturations. In this domain the nucleation process is purely kinetically (rather than thermodynamically) driven with dimer formation being the critical step. In the XS-domain evaporation rates for all clusters are negligible, which implies that the growth of an arbitrary cluster is kinetically controlled by sequences of association (*coalescence*) processes [31].

The details of the combined *MKNT-XS* model used in this study will be presented elsewhere.

Figure 13(a) shows the expected temperature T_N at the exit of the nozzle calculated using the *MKNT-XS* model for various values of stagnation temperature T_0 ranging between 300 K and 450 K. A good agreement between the results of calculations and the experimental observations is evident. Local nucleation rates are also shown in Figs. 13(b) and 13(c), manifesting the effect of the stagnation temperature on the resulting degree of nucleation. All in all, the results obtained indicate that nucleation might well be responsible for the observed discrepancy between the measured Mach number distribution at room temperature and that computed, in which nucleation effects are not taken into account.

VI. SUMMARY AND OUTLOOK

State-of-the-art fluid dynamics calculations were performed to obtain a hypersonic nozzle contour able to produce a very uniform and collimated argon gas jet with $M \approx 8.5$. Inclusion of viscous corrections in these calculations revealed the formation of a thick boundary layer mainly attributed to the specific conditions in typical IGLIS experiments, such as low stagnation gas cell pressures $P_0 = 100$–500 mbar and a small nozzle throat diameter $d = 1$ mm, which result in gas regimes with very low Reynolds numbers.

The resulting contour was machined in an iterative process with the highest accuracy and surface finish using computer numerical control (CNC) technology. Unlike in previous experiments, the mechanical specifications of the nozzles could be adjusted up to their optimal value by the nondestructive molding technique making it possible to perform experiments only with the best nozzles, i.e., with a surface roughness $R_a \leqslant 0.1$ μm and a manufacturing accuracy from the calculated contour $\Delta_c = \pm 5$ μm.

TABLE I. Overview of the results presented in Fig. 10 for the Mach number and the jet temperature obtained by numerical (CFD) simulations as well as the PLIFS and RIS mapping methods for various jet lengths δ, from the nozzle exit, over which the results are averaged. Expected performance in future on-line experiments are indicated by $\delta_2 = 61.5$ mm, which represents the length that should be covered by the lasers to assure the full experimental duty cycle is matched at 10 kHz repetition rate and a stagnation temperature of 380 K. δ_1 and δ_3 are added for comparison.

	$\delta_1 = 50$ mm	$\delta_2 = 61.5$ mm	$\delta_3 = 100$ mm
$\text{Mach}_{\text{Simul.}}$	8.35	8.35	8.35
$T_{\text{Simul.}}$ (K)	15.7	15.7	15.7
Mach_{RIS}	8.22(13)	8.11(12)	7.84(11)
T_{RIS} (K)	16.2(5)	16.6(5)	17.7(5)
$\text{Mach}_{\text{PLIFS}}$	8.15(7)	8.14(6)	7.84(8)
T_{PLIFS} (K)	16.4(3)	16.5(2)	17.7(4)

PLIF measurements were first carried out to obtain matched flow conditions, whereby a highly collimated and uniform density gas jet was observed.

In such working conditions PLIFS measurements were performed to determine the flow velocity and flow temperature along the central line of the jet that could finally be used to map the evolution of the Mach number. Subsequently, we developed and applied a new RIS-based mapping method that reproduced well the results obtained by the PLIFS method. These results, presented in Fig. 10 along with the predictions from CFD calculations, are summarized in Table I and can be used to estimate the expected performance in real experimental conditions at RIB facilities for different average jet distances. These values were computed for the lowest optimal stagnation temperature of 380 K. For this stagnation temperature, the core jet temperature is found to be $T = 16.6(4)$ K and the jet velocity is 615.0(4) m/s, requiring a 61.50(4) mm long laser sheet, at a laser repetition rate of 10 kHz, in order to minimize duty-cycle losses in future experiments with exotic nuclei. An average value $M = 7.84(11)$ [$T = 17.7(5)$ K] for a total distance of 100 mm has been observed taking into consideration the corrections due to the likely mechanical misalignment present in these measurements. These results, therefore, are a proof for future measurements with optimal efficiency and spectral resolution and serve, in addition, to validate the RIS mapping method. The higher detection efficiency and sensitivity (better signal-to-noise ratio) characteristic of ion detection techniques, in contrast to those based on photon detection, make the RIS method to surpass the performance of PLIFS when flow velocity and flow temperature is to be determined with the highest accuracy. Furthermore, unlike in PLIFS, the RIS mapping method offers the possibility of probing the gas jet in any geometrical plane. Nonetheless, we find that both methods complement well, as a first flow visualization by PLIF provides a global jet picture from which matched flow conditions are easily found, paving the way for the following RIS measurements.

It should be noted that besides the low-detection efficiency of photons, the lower overall efficiency of the PLIFS method at the IGLIS laboratory is significantly reduced owing to the small branching ratio of the selected transition in copper. By

selecting a different transition, eventually a different element, this situation could, in the best case be improved from the current ∼2% to ≈100%, which would result in a factor of 50 increase. A further improvement could be reached in the PLIFS method by using a mono-isotopic source, for instance an enriched ^{63}Cu filament, to avoid problems arising from the absence of mass separation. For the RIS method, the transport efficiency of the ions up to the detector could be improved. In general, a stable, easy to produce, isotope of nuclear spin zero with an accessible laser transition would benefit both techniques, as even higher accuracy in the results can be obtained. Altogether, even in optimal conditions the overall efficiency of the RIS method will be at least an order of magnitude better than that of the PLIFS method, which make the former to be better suited to determine the flow properties faster and with a higher accuracy.

The higher sensitivity of the RIS method made it possible to compare between the relative density profiles of filaments F1 and F2 that pointed to the lack of proper diffusion and to the presumption of preferential flow lines in the gas jet associated to the spatial location within the gas cell in which the copper atoms are produced. It is worth noting that such effects might be common in other flow visualization techniques utilizing seeding particles. These observations triggered further investigations of flow properties using F1, i.e., with a stagnation temperature $T_0 \approx 315$ K close to room temperature in contrast to previous studies at $T_0 \approx 480$ K. A systematic increase of the jet temperature, resulting in a decrease of the Mach number, was then observed that could not be reproduced by fluid dynamics calculations. One possible explanation for this behavior was found in the dynamics of nucleation. RIS measurements for different stagnation temperatures show what appears to be an onset of argon nucleation at $T_0 \approx 380$ K that satisfactorily can be explained by our nucleation model. Whereas our modeling indicates that nucleation plays an important role and should carefully be considered when using hypersonic nozzles and argon as the carrier gas, caution is advised as these calculations are based on a number of assumptions, namely (i) nucleation dynamics is decoupled from the gas-dynamics calculations of the flow parameters. This is a rather severe approximation as it is expected that the increase in temperature and effective mass of the carrier gas molecules due to nucleation might influence the flow properties, requiring a fully coupled set of equations, (ii) the present model for T_N ignores cluster evaporation, and (iii) flow lines are discarded in the static 3D integration over the nozzle volume.

The nozzle performance was also tested for different stagnation pressures in view of the future online experiments at the Helmholtzzentrum fuer Schwerionenforschung (GSI) facility, in which in-gas-jet laser spectroscopy will be applied to study the nuclear structure of the ground state and a high-spin K isomer in ^{254}No [9]. Applying the PLIF method and fixing P_{bg} according to the ratio P_0/P_{bg} found in previous measurements for $P_0 = 300$ mbar, we were able to visualize the formation of collimated gas jets for higher P_0 up to $P_0 = 500$ mbar (higher values of P_0 were not tested for being unpractical in online experiments). Similarly, jet formation was observed for lower stagnation pressures down to $P_0 \approx 100$ mbar. For lower values the observed relative density variations along the jet were consistent with a $1/x^2$ intensity decrease, with x the distance from the nozzle, which is characteristic of a flow in free expansion. These results seem to indicate that for values of $P_0 \lessapprox 100$ mbar the resulting low Reynolds number thickens significantly the boundary layer to the extreme of inhibiting jet formation. Once more the difficulties of working with low Reynolds numbers are evident and point to the need of proper viscous corrections to obtain long and uniform jets with high Mach numbers.

For experiments at significantly lower stagnation pressures as those reported here a different nozzle will be implemented. A new set of calculations has recently been performed at VKI and two nozzles have been machined in the same way as that presented in these studies. Tests are ongoing to characterize the performance of these low-pressure nozzles with design conditions M = 8.5, $P_0 = 80$ mbar, $T_0 = 300$, K and $d = 1$ mm. Notice that for this lower stagnation pressure condition a boundary layer roughly twice thicker than that presented here for the nozzle characterized in these studies is expected if we assume that the boundary layer thickness and displacement thickness are inversely proportional to the square root of the Reynolds number.

For stagnation conditions $P_0 \approx 300$ mbar and $T_0 = 380$ K suitable at most radioactive beam facilities, the nozzle presented here assures excellent conditions for gas-jet laser spectroscopy experiments such as a low jet temperature $T \approx 17$ K, a high collimation and flow uniformity. In these conditions, an optimal ionization efficiency and an average spectral resolution ≈170(10) MHz (assuming a typical atomic transition in the UV region at 350 nm) will be feasible in future experiments on the actinides or transactinides with mass numbers in the range A = 205–266.

ACKNOWLEDGMENTS

This work has been funded by FWO-Vlaanderen (Belgium), by GOA/2015/010 (BOF KU Leuven), by the Excellence of Science Research Project, and by a Grant from the European Research Council (No. ERC-2011-AdG-291561-HELIOS). This project has received funding from the European Union's Horizon 2020 research and innovation programme under Grant Agreement No. 654002.

APPENDIX: TEMPERATURE PROFILE IN THE NOZZLE: ACCUMULATED LIQUID MASS APPROACH

Let m_a be the total mass of the seeded isotopes in the jet, m_v be the total mass of the condensible component atoms (argon) in the vapor phase, and m_l be the total mass of the condensible component in the liquid phase. The sum of the masses is constant, i.e., $m_a + m_c = m = \text{const}$, where $m_c = m_v + m_l = \text{const}$ is the total mass of argon. During the condensation process the liquid phase is formed at the expense of the depleting vapor, yielding $dm_l = -dm_v$. The *liquid mass fraction* $g_l = m_l/m$ lies within the range $0 \leqslant g_l \leqslant g_{\max}$, where $g_{\max} = m_c/m$ is the liquid fraction when *all* atoms of the condensible component are in the liquid phase: $m_l = m_c,\ m_v = 0$.

The energy conservation for the steady inviscid flow of the mixture with mass m is given by *Bernoulli's equation* [32]

$$\tfrac{1}{2}m||\vec{u}||^2 + m_a h_a + m_v h_v + m_l h_l = \text{const},$$

where $\vec{u}$ is the flow velocity profile along the nozzle; h_a, h_v, h_l are the specific enthalpies of the mixture components (seeded atoms, argon vapor, argon liquid, respectively). Introducing the latent heat of condensation $L = h_v - h_l$, we rewrite Bernoulli's equation as

$$\frac{1}{2}||\vec{u}||^2 + \left(\frac{m_a}{m}h_a + \frac{m_c}{m}h_v\right) - g_l L = \text{const}. \tag{A1}$$

In the simplest approximation we set $h_a = c_{p,a}T$, $h_v = c_{p,v}T$ where $c_{p,a}$ and $c_{p,v}$ are the specific heats at constant pressure for the seeded atoms and the vapor, respectively. Then, Eq. (A1) takes the form

$$\tfrac{1}{2}||\vec{u}(\vec{z})||^2 + c_{p,0}T(\vec{z}) - g_l(\vec{z})L(\vec{z}) = \text{const}, \tag{A2}$$

where $\vec{z} = (r, \phi, x)$ is an arbitrary point in the nozzle in cylindrical coordinates, $r > 0$ is the radial distance from the nozzle axis x, ϕ is the polar angle and $c_{p,0} = (1 - g_{\max})c_{p,a} + g_{\max}c_{p,v}$.

Equation (A2) should be satisfied at all points $\vec{z}$; in particular for stagnation conditions corresponding to $T = T_0$, $\vec{u} = 0$, $g_l = 0$. Thus, Eq. (A2) takes the form

$$\tfrac{1}{2}||\vec{u}(\vec{z})||^2 + c_{p,0}\,T(\vec{z}) - g_l(\vec{z})\,L(\vec{z}) = c_{p,0}\,T_0. \tag{A3}$$

In order to calculate the liquid mass fraction $g_l(\vec{z})$ we assume that clusters formed by nucleation do not evaporate during their presence in the nozzle. Consider a macroscopically small volume $dV = r\,dr d\phi dx$. The mass of the liquid formed in this volume due to nucleation can be approximated as

$$dm_l \approx m_1 n_c(r, \phi, x)\,J(r, \phi, x)\,\Delta t\,dV. \tag{A4}$$

Here m_1 is the mass of an argon atom, $J(r, \phi, x)$ is the nucleation rate at the point (r, ϕ, x), calculated within a suitable nucleation model (for review see Ref. [28] and references therein), $n_c(r, \phi, x)$ is the number of molecules in the critical cluster, and Δt is a characteristic time during which $J \approx$ const. In the present study we use MKNT [28,30] for nucleation rate calculations. In Eq. (A4) we assumed that all nucleated clusters are of the same size $n_c(r, \phi, x)$. In order to eliminate ambiguity in Δt, it is plausible to define it as the time between consecutive collisions of vapor monomers with the critical cluster: $\Delta t \equiv 1/f(n_c)$, where $f(n)$ is the forward (condensation) rate for the n cluster. Thus, Eq. (A4) can be rewritten as

$$dm_l \approx m_1 n_c(r, \phi, x)\left[\frac{J(r, \phi, x)}{f_c}\right] r dr d\phi dx,$$

where we denoted $f_c = f(n_c(r, \phi, x))$. Neglecting evaporation of clusters and assuming angular symmetry, the liquid mass accumulated at an arbitrary point x' of the nozzle axis can be presented as

$$m_l(x') = m_1 \int_0^{x'} \int_0^{r_c(x)} n_c(r, x)\left[\frac{J(r, x)}{f_c}\right] 2\pi r dr dx,$$

where $r_c(x)$ is the radius of the nozzle contour at a distance x from the throat.

The total mass of the system "seeded atoms + vapor + liquid" contained in the volume bounded by $x = 0$ and the nozzle exit $x = x_F$ is

$$m(x_F) = \int_0^{x_F} \int_0^{r_c(x)} \rho_m(r, x)\,2\pi r dr dx,$$

where ρ_m is the mass density of the system. Then, the liquid mass fraction at the nozzle exit can be approximated as

$$g_l(x_F) \approx \frac{m_1 \int_0^{x_F} \int_0^{r_c(x)} n_c(r, x)\left[\frac{J(r,x)}{f_c}\right] \Theta[J(r, x) - J_0]\, r dr dx}{\int_0^{x_F} \int_0^{r_c(x)} \rho_m(r, x)\,\Theta[J(r, x) - J_0]\, r dr dx}, \tag{A5}$$

where $\Theta(y)$ is the Heaviside unit step-function

$$\Theta(y) = \begin{cases} 0, & y < 0 \\ 1, & y \geqslant 0 \end{cases}$$

and J_0 is a minimum nucleation rate, i.e., the rate corresponding to *appreciable nucleation*. Introduction of this term is aimed at excluding from the total mass [denominator in Eq. (A5)] the contribution of those parts of the nozzle that correspond to negligible nucleation. One can choose J_0 from the condition $J_0 V_{\text{nozzle}}\, t_{\text{res}} \approx 1$, where V_{nozzle} is the nozzle volume and t_{res} is the residence time of the vapor molecules in it. This condition corresponds to formation of one critical cluster in the volume V_{nozzle} during the time t_{res}. For the nozzle used in the present study $J_0 \approx 10\,\text{cm}^{-3}\,\text{s}^{-1}$.

Using (A5), the energy equation (A3) takes the form

$$\frac{1}{2}||u_F||^2 + c_{p,0}T_N - \frac{m_1 \bar{L} \int_0^{x_F} \int_0^{r_c(x)} n_c(r, x)\left[\frac{J(r,x)}{f_c}\right] \Theta[J(r, x) - J_0]\, r dr dx}{\int_0^{x_F} \int_0^{r_c(x)} \rho_m(r, x)\,\Theta[J(r, x) - J_0]\, r dr dx} = c_{p,0}T_0, \tag{A6}$$

where $\vec{u}_F = \vec{u}(x_F, 0)$, $T_N = T(x_F, 0)$ are, respectively, the velocity and temperature at the exit measured at the nozzle axis ($r = 0$). In accordance with our *accumulated liquid mass approach* we replaced the latent heat L by its average over the nozzle volume

$$\bar{L} = \frac{\int_0^{x_F} \int_0^{r_c(x)} L(r, x)\,2\pi r dr dx}{V_{\text{nozzle}}}.$$

From Eq. (A6) the temperature at the exit of the nozzle is

$$T_N = T_0 + \frac{m_1 \bar{L}}{c_{p,0}} \left\{ \frac{\int_0^{x_F} \int_0^{r_c(x)} n_c(r, x)\left[\frac{J(r,x)}{f_c}\right] \Theta[J(r, x) - J_0]\, r dr dx}{\int_0^{x_F} \int_0^{r_c(x)} \rho_m(r, x)\,\Theta[J(r, x) - J_0]\, r\, dr dx} \right\} - \frac{1}{2}\frac{||\vec{u}_F||^2}{c_{p,0}}. \tag{A7}$$

The second term on then right-hand side of this expression represents the temperature increase due to release of latent heat in the process of nucleation.

[1] T. E. Cocolios, A. N. Andreyev, B. Bastin, N. Bree, J. Büscher, J. Elseviers, J. Gentens, M. Huyse, Y. Kudryavtsev, D. Pauwels, T. Sonoda, P. VandenBergh, and P. Van Duppen, Magnetic Dipole Moment of ^{57,59}Cu Measured by In-Gas-Cell Laser Spectroscopy, Phys. Rev. Lett. **103**, 102501 (2009).

[2] R. Ferrer, N. Bree, T. E. Cocolios, I. G. Darby, H. De Witte, W. Dexters, J. Diriken, J. Elseviers, S. Franchoo, M. Huyse *et al.*, In-gas-cell laser ionization spectroscopy in the vicinity of ^{100}Sn: Magnetic moments and mean-square charge radii of N = 50–54 Ag, Phys. Lett. B **728**, 191 (2014).

[3] M. Laatiaoui, W. Lauth, H. Backe, M. Block, D. Ackermann, B. Cheal, P. Chhetri, C. E. Düllmann, P. van Duppen, J. Even, R. Ferrer *et al.*, Atom-at-a-time laser resonance ionization spectroscopy of nobelium, Nature (London) **538**, 495 (2016).

[4] S. Raeder, D. Ackermann, H. Backe, R. Beerwerth, J. C. Berengut, M. Block, A. Borschevsky, B. Cheal, P. Chhetri, C. E. Dullmann, V. A. Dzuba, E. Eliav, J. Even, R. Ferrer, V. V. Flambaum, S. Fritzsche, F. Giacoppo, S. Gotz, F. P. Hessberger, M. Huyse *et al.*, Probing Sizes and Shapes of Nobelium Isotopes by Laser Spectroscopy, Phys. Rev. Lett. **120**, 232503 (2018).

[5] A. Trürler, R. Eichler, and A. Yakushev, Chemical studies of elements with Z $\geqslant$ 104 in gas phase, Nucl. Phys. A **944**, 640 (2015).

[6] Yu. Ts. Oganessian, Sizing up the heavyweights, Nature (London) **413**, 122 (2001).

[7] Yu. Kudryavtsev, R. Ferrer, M. Huyse, P. Van den Bergh, and P. Van Duppen, The in-gas-jet laser ion source: Resonance ionization spectroscopy of radioactive atoms in supersonic gas jets, Nucl. Instrum. Meth. B **297**, 7 (2013).

[8] R. Ferrer, A. Barzakh, B. Bastin, R. Beerwerth, M. Block, P. Creemers, H. Grawe, R. de Groote, P. Delahaye, X. Fléchard *et al.*, Towards high-resolution laser ionization spectroscopy of the heaviest elements in supersonic gas jet expansion, Nat. Commun. **8**, 14520 (2017).

[9] S. Raeder, M. Block, P. Chhetri, R. Ferrer, S. Kraemer, T. Kron, M. Laatiaoui, S. Nothhelfer, F. Schneider, P. Van Duppen *et al.*, A gas-jet apparatus for high-resolution laser spectroscopy on the heaviest elements at SHIP, Nucl. Instrum. Meth. B **463**, 272 (2020).

[10] R. Ferrer, B. Bastin, D. Boilley, P. Creemers, P. Delahaye, E. Lienard, X. Flechard, S. Franchoo, L. Ghys, M. Huyes *et al.*, In gas laser ionization and spectroscopy experiments at the superconducting separator spectrometer (S^3): Conceptual studies and preliminary design, Nucl. Instrum. Methods Phys. Res. B **317**, 570 (2013).

[11] Yu. Kudryavtsev, P. Creemers, R. Ferrer, C. Granados, L. P. Gaffney, M. Huyse, E. Mogilevskiy, S. Raeder, S. Sels, P. Van den Bergh *et al.*, A new in-gas-laser ionization and spectroscopy laboratory for off-line studies at KU Leuven, Nucl. Instrum. Methods Phys. Res. Bs **376**, 345 (2016).

[12] M. Verlinde, R. Ferrer, A. Claessens, C. A. Granados, S. Kraemer, Yu. Kudryavtsev, D. Li, P. Van den Bergh, P. Van Duppen, and E. Verstraelen, Single-longitudinal-mode pumped pulsed-dye amplifier for high-resolution laser spectroscopy, Rev. Sci. Instrum. **91**, 103002 (2020).

[13] S. Sels, R. Ferrer, K. Dockx, C. Granados Buitrago, M. Huyse, Yu. Kudryavtsev, S. Kraemer, S. Raeder, P. Van Den Bergh, P. Van Duppen *et al.*, Design and commissioning of an ion guide system for in-gas laser ionization and spectroscopy experiments, Nucl. Instrum. Methods Phys. Res. B **463**, 148 (2019).

[14] A. Zadvornaya, P. Creemers, K. Dockx, R. Ferrer, L. P. Gaffney, W. Gins, C. Granados, M. Huyse, Y. Kudryavtsev, M. Laatiaoui, E. Mogilevskiy, S. Raeder, S. Sels, P. Van den Bergh, P. Van Duppen, M. Verlinde, E. Verstraelen, M. Nabuurs, D. Reynaerts, and P. Papadakis, Characterization of Supersonic Gas Jets for High-Resolution Laser Ionization Spectroscopy of Heavy Elements, Phys. Rev. X **8**, 041008 (2018).

[15] J. D. Anderson, *Hypersonic and High-Temperature Gas Dynamics,* 2nd ed. (AIAA Education Series, Reston, VA, 2006).

[16] Th. B. Gatski and J-P. Bonnet, Experimental measurement and analysis strategies, in *Compressibility, Turbulence and High Speed Flow,* 2nd ed. (Academic Press, New York, 2013).

[17] W. Tollmien, H. Schlichting, H. Görtler, and F. W. Riegels, *Näherungsverfahren zur zeichnerischen Ermittlung von ebenen Strömungen mit Überschallgeschwindigkeit* (Springer, Berlin, 1961).

[18] J. D. Anderson, *Modern Compressible Flow: With Historical Perspective*, 3rd ed. (McGraw-Hill, New York, 2004).

[19] J. C. Sivells, Aerodynamic design of axisymmetric hypersonic wind tunnel nozzles, J. Spacecr. Rockets **7**, 1292 (1970).

[20] J. Lukasiewicz, *Experimental Methods of Hypersonics* (Marcel Dekker, Inc., New York, 1973).

[21] K. K. Saxena, M. Bellotti, J. Qian, and D. Reynaerts, Characterization of circumferential surface roughness of micro-EDMed holes using replica technology, Procedia CIRP **68**, 582 (2018).

[22] F. Baruffi, P. Parenti, M. Cacciatore, F. ans Annoni, and G. Tosello, On the application of replica molding technology for the indirect measurement of surface and geometry of micromilled components, Micromachines **8**, 195 (2017).

[23] M. Verlinde *et al.*, On the performance of wavelength meters: Part 1—Consequences for medium-to-high-resolution laser spectroscopy, Appl. Phys. B **126**, 85 (2020).

[24] K. Dockx, S. Geldhof, K. König, D. Studer, T. E. Cocolios, R. P. de Groote, R. Ferrer, Yu. Kudryavtsev, T. Kieck, I. Moore *et al.*, A new control system for high-precision in-gas laser ionization and spectroscopy experiments at KU Leuven, Nucl. Instrum. Methods Phys. Res. B **463**, 297 (2020).

[25] R. P. de Groote, M. Verlinde, V. Sonnenschein, K. T. Flanagan, I. Moore, and G. Neyens, Efficient, high-resolution resonance laser ionization spectroscopy using weak transitions to long-lived excited states, Phys. Rev. A **95**, 032502 (2017).

[26] M. Verlinde, Towards the in-gas jet laser ionization spectroscopy of the ^{229}Th isomer, Ph.D. thesis, Katholieke Universiteit Leuven, 2021.

[27] E. Verstraelen, Laser spectroscopy of actinides: Octupole deformation and gas-jet characterization, Ph.D. thesis, Katholieke Universiteit Leuven, 2021.

[28] V. I. Kalikmanov, *Nucleation Theory* (Springer, Dordrecht, 2013).

[29] S. Sinha, A. Bhabhe, H. Laksmono, J. Wölk, R. Strey, and B. Wyslouzil, Argon nucleation in a cryogenic supersonic nozzle, J. Chem. Phys. **132**, 064304 (2010).

[30] V. I. Kalikmanov, Mean-field kinetic nucleation theory, J. Chem. Phys. **124**, 124505 (2006).

[31] V. I. Kalikmanov and R. Hagmeijer, Cluster formation at extreme supersaturations: Nucleation versus barrierless transition, J. Phys. Chem. B **123**, 10890 (2019).

[32] P. P. Wegener, Gasdynamics of expansion flows with condensation and homogeneous nucleation of water vapor, in *Nonequilibrium Flows, Part I, Vol. 1 of Gasdynamics* (Marcel Dekker, New York, 1969).